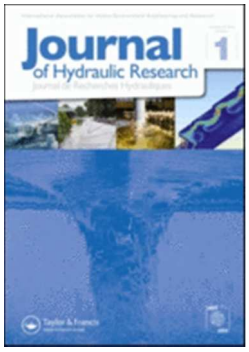

Development of roll-waves in power-law fluids with non-uniform initial conditions

Journal:	*Journal of Hydraulic Research*
Manuscript ID	TJHR-2015-0096.R3
Manuscript Type:	Research paper
Date Submitted by the Author:	07-Jan-2016
Complete List of Authors:	Campomaggiore, Francesca; Universita degli Studi di Trieste Dipartimento di Ingegneria e Architettura, Dipartimento di Ingegneria e Architettura Di Cristo, Cristiana; Università di Cassino e del Lazio Meridionale, Dipartimento di Ingegneria Civile e Meccanica Iervolino, Michele; Seconda Università degli Studi di Napoli, Dipartimento di Ingegneria Civile, Design, Edilizia e Ambiente Vacca, Andrea; Seconda Università degli Studi di Napoli,, Dipartimento di Ingegneria Civile, Design, Edilizia e Ambiente
Keywords:	roll-waves, surface instability, gradually varied profile, power-law fluid, shock-capturing method
JHR Keywords:	Flow instabilities, Non-Newtonian fluid flows, One-dimensional models < Computational methods in hydro-environment research and fluid dynamics, Shallow flows < Environmental Fluid Mechanics

Development of roll-waves in power-law fluids with non-uniform initial conditions

FRANCESCA CAMPOMAGGIORE, PhD Student, *Dipartimento di Ingegneria e Architettura, Università di Trieste, Trieste, Italy*

Email: francesca.campomaggiore@phd.units.it

CRISTIANA DI CRISTO (IAHR Member), Assistant Professor, *Dipartimento di Ingegneria Civile e Meccanica, Università di Cassino e del Lazio Meridionale, Cassino (FR), Italy*

Email: dicristo@unicas.it

MICHELE IERVOLINO (IAHR Member), Assistant Professor*, Dipartimento di Ingegneria Civile, Design, Edilizia e Ambiente, Seconda Università di Napoli, Aversa (CE), Italy*

Email: michele.iervolino@unina2.it *(author for correspondence)*

ANDREA VACCA, Associate Professor, *Dipartimento di Ingegneria Civile, Design, Edilizia e Ambiente, Seconda Università di Napoli, Aversa (CE), Italy*

Email: vacca@unina.it

Running Head: Roll-waves in non-uniform power-law flows

Development of roll-waves in power-law fluids with non-uniform initial conditions

ABSTRACT

The paper investigates the spatial evolution of a disturbance in an open-channel flow of a power-law fluid at non-uniform accelerated and decelerated initial profiles, up to the occurrence of roll-waves in mild and steep slope channels. Both theoretical and numerical analyses are applied to the depth-averaged continuity and momentum conservation equations, deduced from the von Kármán's integral method. For the theoretical investigation, the non-linear near-front expansion technique has been applied. Then, the full non-linear problem in its conservative formulation has been numerically solved. Independently on the rheology of the flowing medium, non-uniform initial conditions strongly influence the perturbation celerity, the disturbance evolution and the roll-waves development. For mild slope channels, an initially decelerated profile of shear-thinning fluids has a stabilizing effect, while the opposite is found for accelerated profiles. For shear-thickening fluids, only the stabilizing effect caused by a decelerated profile is observed. In steep slope channels, independently of the fluid rheology, decelerated initial conditions promote the roll-wave occurrence, while accelerated ones inhibit the perturbation growth. Although experimental verifications are needed, present results have to be properly accounted in defining roll-waves prediction methods and in assigning appropriate boundary conditions to enhance or to reduce their formation.

Keywords: Gradually varied profile; power-law fluid; roll-wave; shock-capturing method; surface instability.

1 Introduction

Steady flow of thin layer of fluids with various rheologies in an inclined open channel may become unstable under certain conditions, up to the occurrence of surface waves which wavelength largely exceeds the layer thickness. Such a long-wave instability may degenerate into a series of progressing bores, known as roll-waves. The control of this instability concerns many processes involving both Newtonian and non-Newtonian fluids. In environmental hydraulics, water or muddy intermittent flows often occur in rivers, with clay/water mixture especially observed after torrential rains (Takahashi, 1991). Moreover, the formation of intermittent waves may follow volcano eruptions in magma (Kang & Chen, 1995), which behaves as a non-Newtonian fluid (Pinkerton & Sparks, 1978). In several industrial applications large-amplitude superficial waves in non-Newtonian fluids can be useful, since they facilitate the mixing and in turn the mass and heat exchange; conversely, in other ones the interfacial instability would deteriorate the process performance, e.g. causing an uneven distribution of material in coating applications. The present paper aims to investigate the effect of initial gradually varied profiles, which characterize physical systems,

on the roll-waves development in the flow of a non-Newtonian fluid.

For describing the behaviour of non-Newtonian fluids, rheological models accounting for the presence of a yield stress have been proposed. Indeed several linear, i.e. Bingham (e.g., Trowbridge, 1987; Liu & Mei, 1989; Liu & Mei, 1990; Balmforth & Craster, 1999; Mei & Yuhi, 2001; Hewitt & Balmforth, 2013) and non-linear, i.e. Herschel & Bulkley (e.g., Coussot, 1994; Huang & Garcia, 1998; Balmforth & Liu, 2004; Chanson, Jarny & Coussot, 2006; Di Cristo, Iervolino & Vacca, 2013a, 2013b, 2013c; Di Cristo, Iervolino & Vacca, 2014) models have been used. In addition, the power-law fluid model, which does not account for the yield stress, remains one of the most widely adopted with either shear-thinning (n<1, n is the rheological index) or shear-thickening (n>1) behaviour. Such a model is particularly well-suited for analyzing fine sediment-water mixtures, magmas and mining residuals when the yield stress is negligible (e.g., Ng & Mei, 1994; Sonder, Zimanowski & Buttner, 2006; Burger, Haldenwang & Alderman, 2010; Longo, Di Federico & Chiapponi, 2015).

Several laboratory experiments (e.g., Coussot, 1994; Wang, 2002; Forterre & Pouliquen, 2003) have shown that the roll-waves occurrence in non-Newtonian fluids, similarly to the clear-water in turbulent regime, is strictly related to surface instability, which, spatially growing along the channel, finally leads to the formation of shock waves. Such an observation prompted many researchers to the theoretical study of roll-waves formation through the stability analysis of the flow model, with either linear or quasi-linear approaches.

In the framework of the long-wave approximation, the linear stability of a uniform flow of power-law fluid over an inclined plane has been investigated by Ng and Mei (1994), using the von Kármán's integral method. Ng and Mei (1994) carried out a rigorous stability analysis for Reynolds number order of one showing that the von Kármán approximation adequately describes the essential features of both linear and non-linear instability. Hwang, Chen, Wang and Lin (1994) included the surface tension effect in the Ng and Mei (1994) model and enlightened that a decrease of the Weber number destabilizes the flow. The long-wave perturbation along with the multiple scales method has been employed by Lin and Hwang (2000) to derive a non-linear evolution equation of film thickness. The results revealed that the system is more unstable when power-law exponent decreases. With reference to the flow model of Hwang et al. (1994), Dandapat and Mukhopadhyay (2001, 2003) pointed out the role of both kinematic and dynamic waves, which may act together or individually to dominate the flow field. Miladinova, Lebon and Toshev (2004) investigated, using Benney's long-wave approach, the non-linear evolution of falling uniform films of a power-law fluid flow over an inclined impermeable wall. Numerical simulations have shown that a non-linear interaction saturates up to the formation of a finite-amplitude permanent wave. Longo (2011) studied finite-amplitude permanent roll-waves in a shallow layer of down-sloping dry granular materials in a dense regime, rheologically described as a shear-

thickening medium (Bagnold, 1954; Chen & Ling, 1996, 1998; Hunt, Zenit, Campbell & Brennen, 2002). Using the simplified von Kàrmàn's momentum integral approach, the Author detected the conditions for the existence of a periodic discontinuous solution, constituted by smooth profiles with a monotonically increasing depth between periodic shocks.

Following the weighted-residual technique originally introduced for Newtonian fluids by Ruyer-Quil and Manneville (1998, 2000), more complex models have been recently proposed to deeply analyze the motion of non-Newtonian films. Fernandez-Nieto, Noble and Villa (2010) provided a consistent thin-layer theory for power-law fluids considering an asymptotic expansion of the solution of the Cauchy momentum equations in the shallow-water scaling and in the neighbourhood of the steady solution. Bouchut and Boyaval (2013) proposed a reduced form of the Upper-Convected Maxwell equations for viscoelastic fluids valid in general geometries. Noble and Villa (2013) developed a model for a power-law fluid through a second-order asymptotic expansion of the fluid velocity field and fluid strain in the shallow-water regime. Finally, Bouchut and Boyaval (2016) have proposed a unified approach for several fluid models for thin-layer regime based on a mathematical coherence property, which defines a reduced model when the rheology is specified.

The modifications of the stability limit in a power-law film caused by the presence of additional external forcing, such as wind stress (e.g., Pascal & D'Alessio, 2007; Uma, 2012), bed porosity (e.g., Pascal, 2006; Sadiq & Usha, 2010; Usha, Millet, Ben Hadid & Rousset, 2011; Di Cristo, Iervolino & Vacca, 2013d), the waviness bottom (e.g., Heining & Aksel, 2010), have been investigated as possible ways to control, i.e. to inhibit or to enhance, the roll-waves occurrence. In particular, Usha et al. (2011) carried out a temporal stability analysis perturbing the two-dimensional Cauchy Momentum Equations coupled with the power-law rheological model, i.e. an Orr-Sommerfeld type analysis, in presence of both permeable and impermeable walls. In order to overcome the problem of the power-law flow model related to the divergence of effective viscosity at the free-surface of the film, a Carreau rheological model (Carreau, DeKee & Daroux, 1979) has been considered. With reference to an impermeable bottom, the Authors recovered the power-law model stability limit as an asymptotic behaviour of the Carreau fluid, deducing the limit condition predicted by the rigorous stability analysis of Ng and Mei (1994). This result indirectly confirms the ability of the depth-integrated approach in capturing the essential features of long-wave instability in thin liquid films, coherently with the conclusion of Smith (1990) for Newtonian fluid.

Independently of the flow model considered to describe the dynamics of a power-law film, all the previous studies dealt with a uniform initial condition. However, this condition is essentially a mathematical abstraction, because in a real physical system the hypocritical (respectively hypercritical) flow profile may differ, even strongly, from the uniform one, depending on the boundary condition at the channel outlet (respectively inlet). With reference

to a Bingham fluid, recent experiments (Tamburrino & Ihle, 2013) have shown that the free-surface profile influences the roll-waves occurrence. From the theoretical point of view, for a turbulent Newtonian flow, the effect of gradually-varying depth profiles on the stability limit was enlightened by Dracos and Glenne (1967). Considering the spatial evolution of a wavefront determined by a discontinuity of the free-surface slope in the Saint-Venant model, the Authors showed that the accelerating or decelerating character of the initial profile strongly affects the linear stability condition. These results have been confirmed by Kranenburg (1990) through a multiple scaling technique. With reference to the kinematic wave approximation of the Saint-Venant equations, the fundamental role of small non-uniformities on free-surface has been shown by Bohorquez (2010). It has been found that an initial condition with positive local free-surface slope is more stabilizing than a uniform one. The effects of an initial profile on a mud film, in mild slope channels, have been recently analyzed by Di Cristo, Iervolino and Vacca (2015) considering a Herschel & Bulkley fluid within the Saint-Venant framework (Ancey, 2007). It has been found that in hypocritical conditions, which are often encountered in mud-flows even in conjunction with roll-wave development, a proper choice of the outflow conditions, for instance able to induce a deceleration (respectively an acceleration) of the current, could prevent (respectively promote) the development of instabilities. The above literature review shows that, as far as power-law fluids are concerned, the influence of non-uniform initial profiles on the roll-waves occurrence has not been analysed so far, although the problem is relevant in both environmental and industrial applications.

In the present paper the occurrence of roll-waves in a power-law film with a gradually varying initial profile is investigated. The study considers the hyperbolic flow model proposed by Ng and Mei (1994), which, despite not being the most rigorous one, represents a good trade-off between the physics description and the mathematical complexity. Supported also by the convective character of the instability (Di Cristo et al., 2013d), the near-front expansion technique (Witham, 1974) is applied to study the linear and non-linear spatial evolution of a disturbance, assuming both hypocritical and hypercritical initial profiles. Fully non-linear numerical simulations are carried out in order to confirm the achievements of the theoretical analysis. Even if no comparison is performed within this paper with the scarce experimental available data relative to the influence of gradually varying initial profiles on the propagation of disturbances in power law fluids, the present study furnishes some useful information about the effect of boundary conditions .

The paper is structured as follows. In Section 2 the governing equations are reported. Then the near-front expansion analysis is presented in Section 3, whereas the corresponding results are discussed in Section 4. Section 5 shows the results of the numerical simulations of the fully non-linear problem. Finally, conclusions are drawn in Section 6.

2 Governing equations

Let us consider the two-dimensional laminar flow of a thin layer of power-law fluid over an impermeable fixed wall inclined at angle θ with respect to the horizontal plane (Fig. 1), without any lateral inflow or outflow. The flow resistances by the sidewalls are neglected with respect to those arising from the bottom. Assuming the longitudinal characteristic length of the flow to be much larger than the characteristic depth, measured along the $\tilde{z}$ axis normal to the plane bed, the application of von Kármán's integral method leads to the following depth-integrated continuity and streamwise momentum conservation equations (Ng & Mei, 1994):

$$\frac{\partial \tilde{h}}{\partial \tilde{t}} + \frac{\partial}{\partial \tilde{x}}\left(\tilde{u}\tilde{h}\right) = 0 \tag{1}$$

$$\frac{\partial}{\partial \tilde{t}}\left(\tilde{u}\tilde{h}\right) + \frac{\partial}{\partial \tilde{x}}\left(\beta \tilde{h}\tilde{u}^2\right) - g\tilde{h}\left(\sin\theta - \cos\theta \frac{\partial \tilde{h}}{\partial \tilde{x}}\right) + \frac{\tilde{\tau}_b}{\rho} = 0 \tag{2}$$

in which $\tilde{x}$ and $\tilde{t}$ are the streamwise coordinate and the time, respectively, $\tilde{h}$ is the flow depth, $\tilde{u}$ is the depth-integrated streamwise velocity component, $\tilde{\tau}_b$ is the bottom stress, g and ρ are the gravity and the fluid density, respectively. Figure 1 provides a sketch explaining these variables:

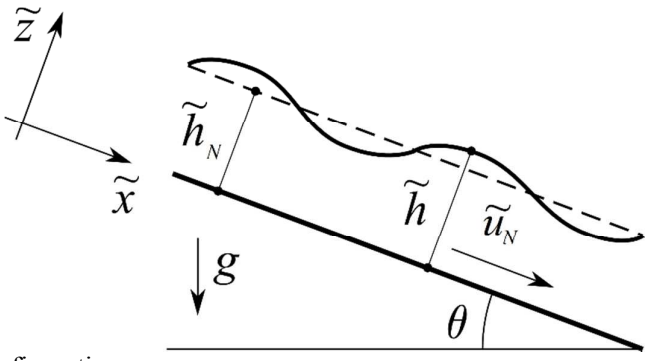

Figure 1 Flow configuration.

A power-law rheology is considered, which describes adequately fluids without appreciable yield stress, such as clay or kaolin suspensions. Adopting the model proposed by Ng and Mei (1994), the momentum correction factor β is expressed as:

$$\beta = 2\frac{2n+1}{3n+2} > 1 \tag{3}$$

and the bottom stress reads:

$$\tilde{\tau}_b = \mu_n \left(\frac{2n+1}{n} \frac{\tilde{u}}{\tilde{h}} \right)^n \tag{4}$$

where n and μ_n are the exponent and the consistency of the power-law fluid, respectively. If the fluid behavior is shear-thinning then $n < 1$, whereas $n > 1$ corresponds to a shear-thickening medium. Setting $n = 1$, the Newtonian case is recovered, with the consistency coinciding with the viscosity. Denoting with $\tilde{h}_N$ the uniform flow depth, the corresponding depth-averaged velocity $\tilde{u}_N$ becomes:

$$\tilde{u}_N = \frac{n}{2n+1} \left(\frac{\rho g \tilde{h}_N^{n+1} \sin\theta}{\mu_n} \right)^{\frac{1}{n}} \tag{5}$$

The following dimensionless variables are introduced:

$$h = \frac{\tilde{h}}{\tilde{h}_N}, \; x = \frac{\tilde{x}}{\tilde{l}_N}, \; t = \frac{\tilde{u}_N}{\tilde{l}_N} \tilde{t} \; , u = \frac{\tilde{u}}{\tilde{u}_N} \tag{6}$$

where $\tilde{l}_N = \tilde{h}_N \cot\theta$. Accounting for definitions (6), the dimensionless form of Eqs (1) and (2), in terms of the primitive variables, $\mathbf{u}^T=(h, u)$ reads:

$$\frac{\partial \mathbf{u}}{\partial t} + \mathbf{A}(\mathbf{u}) \frac{\partial \mathbf{u}}{\partial x} = \mathbf{s}(\mathbf{u}) \tag{7}$$

with:

$$\mathbf{A}(\mathbf{u}) = \begin{bmatrix} u & h \\ (\beta-1)\dfrac{u^2}{h} + \dfrac{1}{\mathsf{F}_N^2} & (2\beta-1)u \end{bmatrix}, \; \mathbf{s}(\mathbf{u}) = \begin{bmatrix} 0 \\ \dfrac{1}{\mathsf{F}_N^2}\left(1 - \dfrac{\tau_b}{h}\right) \end{bmatrix} \tag{8}$$

where τ_b is the dimensionless bottom stress and F_N denotes the Froude number at the uniform condition, expressed, respectively, by:

$$\tau_b = \left(\frac{u}{h} \right)^n, \qquad \mathsf{F}_N = \frac{\tilde{u}_N}{\sqrt{g \tilde{h}_N \cos\theta}} \tag{9}$$

It is easy to verify that the Eqs (7) and (8) consitute a hyperbolic system and that the slopes of the two characteristic lines in the (t, x) phase plane, i.e. the eigenvalues of the **A** matrix, are:

$$\lambda^{\pm} = \beta u \pm \sqrt{\beta(\beta-1)u^2 + \frac{h}{\mathsf{F}_N^2}} \tag{10}$$

whereas the corresponding left eigenvectors read:

$$\mathbf{e}^{\pm} = \begin{bmatrix} \pm(\beta-1)\dfrac{u}{h} - \dfrac{1}{h}\sqrt{\beta(\beta-1)u^2 + \dfrac{h}{\mathsf{F}_N^2}} \\ 1 \end{bmatrix} \tag{11}$$

Owing to the presence of the momentum correction coefficient, differently of the clear-water turbulent case, i.e. the Saint-Venant equations, a closed form of the Riemann invariants is not available, not even for the simple cross-section geometry considered herein.

In the assumed initial steady state condition, henceforth denoted with subscript 0, the flow depth and the velocity have to satisfy the steady-state counterpart of Eq. (7):

$$\mathbf{A}_0 \frac{\mathrm{d}\,\mathbf{u}_0}{\mathrm{d}\,x} = \mathbf{s}_0 \tag{12}$$

in which the expressions of $\mathbf{A}_0$ and of $\mathbf{s}_0$ follow from (8) setting $\mathbf{u}=\mathbf{u}_0(x)$ and read:

$$\mathbf{A}_0 = \begin{bmatrix} u_0 & h_0 \\ (\beta-1)\dfrac{u_0^2}{h_0} + \dfrac{1}{\mathsf{F}_N^2} & (2\beta-1)u_0 \end{bmatrix}, \qquad \mathbf{s}_0 = \begin{bmatrix} 0 \\ \dfrac{1}{\mathsf{F}_N^2}\left(1 - \dfrac{\tau_{b0}}{h_0}\right) \end{bmatrix} \tag{13}$$

The dimensionless bottom stress τ_{b0} is expressed by Eq. (9) with flow variables evaluated in steady conditions. Even if not explicitly indicated $\mathbf{A}_0$ and of $\mathbf{s}_0$ are function of the streamwise coordinate through h_0, u_0 and τ_{b0}.

Equations (12) and (13) show that in the absence of any lateral inflow or outflow, steady flow profiles have a constant flow rate (for unit width), corresponding to the uniform flow value $\widetilde{q}_N = \widetilde{h}_N \widetilde{u}_N$. Therefore, the continuity requirement in dimensionless variables reads:

$$u_0 = \frac{1}{h_0} \tag{14}$$

Accounting for Eq. (14), the system (12) may be rewritten in terms only of the flow depth $h_0(x)$ as follows:

$$\frac{\mathrm{d}\,h_0}{\mathrm{d}\,x} = \frac{1}{h_0^{\,2(n-1)}} \frac{h_0^{\,2n+1} - 1}{h_0^{\,3} - \beta\mathsf{F}_N^2} \tag{15}$$

Similarly to the turbulent clear-water case, denoting with $h_c = \sqrt[3]{\beta\mathsf{F}_N^2}$ the dimensionless critical depth and with $\mathsf{F}_{N,c} = 1/\sqrt{\beta}$ the corresponding critical Froude number value, a mild (respectively steep) slope channel is found whenever $\mathsf{F}_N < \mathsf{F}_{N,c}$, i.e. $h_c < 1$ (respectively $\mathsf{F}_N > \mathsf{F}_{N,c}$, i.e. $h_c > 1$). The critical slope channel case in what follows is not discussed.

Equation (15) states that, for fixed values of the power-law exponent n and normal Froude number F_N, the sign of $\mathrm{d}h_0/\mathrm{d}x$ is function only of the flow depth itself. As it will be shown in the next sections, such a relation plays a key role in the stability of the initial gradually profile. In order to enlighten this aspect, in Fig. 2a the r.h.s. of Eq. (15) is represented for a shear-thinning fluid (i.e. n=0.2, $\mathsf{F}_{N,c}$~0.96), for both mild ($\mathsf{F}_{N,c}$=0.50) and steep ($\mathsf{F}_{N,c}$=1.50) slope channels. Figures 2b and 2c are the counterparts of Fig. 2a for the Newtonian fluid (n=1.0, $\mathsf{F}_{N,c}$~0.91) and for a shear-thickening fluid (n=1.5, $\mathsf{F}_{N,c}$~0.89), respectively. The considered power-law exponent value for the shear-thinning fluid is representative of natural estuarine muds dredged from Haihe River in Tianjin and Mazhou Island near Shenzhen (Zhang, Bai & Ng, 2010), whereas the value selected for the shear-thickening fluid describes the rheology of dry granular flows (Chen & Ling, 1996; Chen & Ling, 1998; Hunt, Zenit, Campbell & Brennen, 2002). It is worth noting that also artificial fluids may exhibit the same rheological behavior. For instance, kaolinite suspensions with volume concentration of 10% are characterized by n~0.2 (Ng & Mei, 1994), whereas mixtures of water with cornstarch concentration of about 60% in weight present n~1.5 (Longo et al., 2015).

As expected from Eq. (15), independently of the n value, for high value of h_0 $\mathrm{d}h_0/\mathrm{d}x$ tends to one, whereas it diverges at the critical flow depth value. The main difference between Figs. 1a, 1b and 1c occurs for small h_0 values. Indeed, for flow depth tending to zero, inspection of Eq. (15) leads to conclude that if n<1 $\mathrm{d}h_0/\mathrm{d}x$ vanishes, while it diverges for n>1. A finite value, i.e. $1/\left(\beta\mathsf{F}_N^2\right)$, is attained in the Newtonian case. Such a difference has a non-negligible effect on the stability of the initial profile, as it will be shown in the next sections.

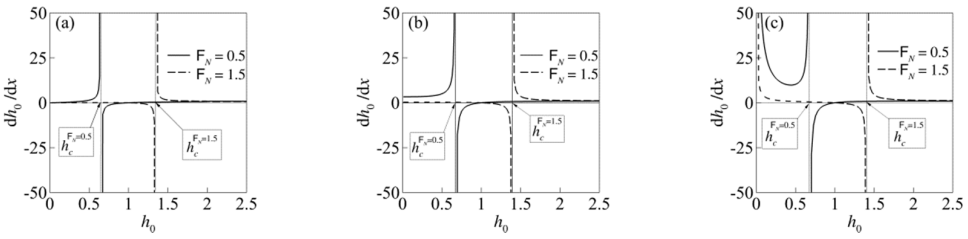

Figure 2 Flow depth x-derivative as a function of the flow depth for mild and steep channels. (a) shear-thinning fluid (n=0.2); (b) Newtonian fluid (n=1); (c) shear-thickening fluid (n=1.5).

3 Near-front expansion analysis

In its essential form, the near-front expansion analysis considers the initial profile perturbed by a jump discontinuity in the first derivative of flow variables. However, higher-order derivatives and other singularities can be in principle handled (Witham, 1974). Owing to the hyperbolic character of system (7)-(8), the discontinuities in the first derivative of **u** propagate along the characteristics and the equation governing their magnitude evolution can be obtained through a change of variable. Such a technique has been successfully applied for studying the stability of gradually-varying initial profiles by Dracos and Glenne (1967) for clear-water in turbulent regime, and by Di Cristo et al. (2015) for a Herschel & Bulkley fluid. Compared to these two rheologies, the power-law fluid model introduces two substantial differences: the bottom stress law and the momentum correction coefficient $\beta \neq 1$, which affects the expression of characteristic lines (Eq. 10). Therefore, the results of above cited studies cannot be straightforwardly applied to the power-law case.

The following variables transformation is introduced:

$$\xi = x, \quad \mathrm{d}\eta = \lambda_0^+ \,\mathrm{d}t - \mathrm{d}x \tag{16}$$

with $\lambda_0^+ = \lambda_0^+(\xi)$ denoting the maximum characteristic slope evaluated in the initial condition:

$$\lambda_0^+ = \beta u_0 + \sqrt{\beta(\beta-1)u_0^2 + \frac{h_0}{\mathsf{F}_N^2}} \tag{17}$$

Accounting for Eq. (16), the following identities hold:

$$\frac{\partial \mathbf{u}}{\partial t} = \lambda_0^+ \frac{\partial \mathbf{u}}{\partial \eta}, \qquad \frac{\partial \mathbf{u}}{\partial x} = \frac{\partial \mathbf{u}}{\partial \xi} - \frac{\partial \mathbf{u}}{\partial \eta} \tag{18}$$

and therefore system (7) may be rewritten in the new variables as:

$$\lambda_0^+ \frac{\partial \mathbf{u}}{\partial \eta} + \mathbf{A}(\mathbf{u})\left(\frac{\partial \mathbf{u}}{\partial \xi} - \frac{\partial \mathbf{u}}{\partial \eta}\right) = \mathbf{s}(\mathbf{u}) \tag{19}$$

A convenient way to analyze the evolution of a pointwise perturbation is to expand in series the unknown vector **u** behind the wavefront, i.e. around $\eta = 0$ (Dracos & Glenne, 1967):

$$\mathbf{u}(\xi,\eta) = \mathbf{u}(\xi,0) + \left.\frac{\partial \mathbf{u}}{\partial \eta}\right|_{\eta=0} \eta + \left.\frac{\partial^2 \mathbf{u}}{\partial \eta^2}\right|_{\eta=0} \frac{\eta^2}{2} + \ldots \tag{20}$$

or equivalently:

$$\mathbf{u} = \mathbf{u}_0(\xi) + \mathbf{u}_1(\xi)\eta + \mathbf{u}_2(\xi)\eta^2 + \ldots \tag{21}$$

Similarly, the matrix **A** and the source term **s** are expanded in Taylor series as follows:

$$\mathbf{A} = \mathbf{A}_0(\xi) + \mathbf{A}_1(\xi)\eta + \ldots \tag{22}$$

$$\mathbf{s} = \mathbf{s}_0(\xi) + \mathbf{s}_1(\xi)\eta + \ldots \tag{23}$$

where $\mathbf{A}_0(\xi)$ and $\mathbf{s}_0(\xi)$ are given by Eq. (13), whereas $\mathbf{A}_1(\xi)$ and $\mathbf{s}_1(\xi)$ have the following expressions, in which the dependency from ξ is omitted to simplify the notation:

$$\mathbf{A}_1(\xi) = \begin{bmatrix} u_1 & h_1 \\ (\beta-1)\left(2\dfrac{u_0}{h_0}u_1 - \dfrac{u_0^2}{h_0^2}h_1\right) & (2\beta-1)u_1 \end{bmatrix} \tag{24}$$

$$\mathbf{s}_1(\xi) = \begin{bmatrix} 0 \\ -\dfrac{1}{\mathsf{F}_N^2}\left(\dfrac{\partial}{\partial h}\dfrac{\tau_b}{h}\bigg|_0 h_1 + \dfrac{\partial}{\partial u}\dfrac{\tau_b}{h}\bigg|_0 u_1\right) \end{bmatrix} \tag{25}$$

Accounting for the bottom stress relation (9), the derivatives in Eq. (25) read:

$$\frac{\partial}{\partial h}\frac{\tau_b}{h}\bigg|_0 = -(n+1)\frac{u_0^n}{h_0^{n+2}}, \quad \frac{\partial}{\partial u}\frac{\tau_b}{h}\bigg|_0 = n\frac{u_0^{n-1}}{h_0^{n+1}} \tag{26}$$

Substituting Eqs (21)-(23) in Eq. (19), the following system is obtained:

$$\begin{aligned} &\lambda_0^+\frac{\partial}{\partial\eta}\left[\mathbf{u}_0 + \mathbf{u}_1\eta + \mathbf{u}_2\eta^2 + \ldots\right] + \left[\mathbf{A}_0 + \mathbf{A}_1\eta + \ldots\right]\frac{\partial}{\partial\xi}\left[\mathbf{u}_0 + \mathbf{u}_1\eta + \mathbf{u}_2\eta^2 + \ldots\right] + \\ &- \left[\mathbf{A}_0 + \mathbf{A}_1\eta + \ldots\right]\frac{\partial}{\partial\eta}\left[\mathbf{u}_0 + \mathbf{u}_1\eta + \mathbf{u}_2\eta^2 + \ldots\right] = \mathbf{s}_0 + \mathbf{s}_1\eta + \ldots \end{aligned} \tag{27}$$

Accounting for Eq. (12) the system (27) at the zero-th order of η leads to the following one:

$$\left(\mathbf{A}_0 - \lambda_0^+\mathbf{I}\right)\mathbf{u}_1 = 0 \tag{28}$$

in which **I** denotes the identity matrix. Since λ_0^+ is an eigenvalue of $\mathbf{A}_0$, the system (28) has a rank deficient matrix and $\mathbf{u}_1$ represents the right eigenvector of $\mathbf{A}_0$. It is easy to verify that, accounting for Eq. (17), all the solutions of Eq. (28) have to satisfy the following condition:

$$u_1 = \frac{h_1}{h_0}\left[(\beta-1)u_0 + \sqrt{\beta(\beta-1)u_0^2 + \frac{h_0}{\mathsf{F}_N^2}}\right] \tag{29}$$

At the first order of η the system (27) leads to the following one:

$$2\left(\lambda_0^+\mathbf{I}-\mathbf{A}_0\right)\mathbf{u}_2+\mathbf{A}_0\frac{\mathrm{d}\mathbf{u}_1}{\mathrm{d}\xi}+\mathbf{A}_1\frac{\mathrm{d}\mathbf{u}_0}{\mathrm{d}\xi}-\mathbf{A}_1\mathbf{u}_1=\mathbf{s}_1 \tag{30}$$

Pre-multiplying both left and right sides for the transpose of the left eigenvector $\mathbf{e}_0^+$ of $\mathbf{A}_0$:

$$\mathbf{e}_0^+=\begin{bmatrix}(\beta-1)\frac{u_0}{h_0}-\frac{1}{h_0}\sqrt{\beta(\beta-1)u_0^2+\frac{h_0}{\mathsf{F}_N^2}}\\ 1\end{bmatrix} \tag{31}$$

the following equation is deduced:

$$\mathbf{e}_0^+\left(\mathbf{A}_0\frac{\mathrm{d}\mathbf{u}_1}{\mathrm{d}\xi}+\mathbf{A}_1\frac{\mathrm{d}\mathbf{u}_0}{\mathrm{d}\xi}-\mathbf{A}_1\mathbf{u}_1\right)^T=\mathbf{s}_1^T\mathbf{e}_0^+ \tag{32}$$

Accounting for expressions (13), (15), (24), (25), (29) and (31), Eq. (32) may be rewritten in terms of the h_1 function only as follows:

$$f_1\frac{\mathrm{d}h_1}{\mathrm{d}\xi}-f_2{h_1}^2+\left(f_3\frac{\mathrm{d}h_0}{\mathrm{d}\xi}+f_4\right)h_1=0 \tag{33}$$

where:

$$f_1=f_1(\xi)=2\frac{\lambda_0^+}{h_0^2}\left(\lambda_0^+h_0-\beta\right) \tag{34}$$

$$f_2=f_2(\xi)=2\lambda_0^+\frac{\lambda_0^+h_0-2\beta^2}{h_0^3}+2\frac{\beta^2}{h_0^4}-\frac{3+2\beta}{h_0\mathsf{F}_N^2} \tag{35}$$

$$f_3=f_3(\xi)=\frac{1}{2\mathsf{F}_N^2h_0\left(\beta-\lambda_0^+h_0\right)}\left[\frac{\lambda_0^+\left[8\mathsf{F}_N^2\beta(\beta-1)-h_0^3\right]}{h_0^2}+6\beta\right] \tag{36}$$

$$f_4=f_4(\xi)=\frac{n\left(\lambda_0^+h_0-2\right)-1}{\mathsf{F}_N^2{h_0}^{2n+2}} \tag{37}$$

Equation (33) may be finally rewritten in the following compact form:

$$\frac{\mathrm{d}h_1}{\mathrm{d}\xi}-\alpha(\xi)h_1(\xi)^2-\gamma(\xi)h_1(\xi)=0 \tag{38}$$

in which:

$$\alpha(\xi)=\frac{f_2(\xi)}{f_1(\xi)},\ \gamma(\xi)=-\frac{1}{f_1(\xi)}\left[f_3(\xi)\frac{\mathrm{d}h_0}{\mathrm{d}\xi}+f_4(\xi)\right] \tag{39}$$

It is worth noting that in Eq. (39) both α and γ functions depend on ξ only through the gradually varying initial profile $h_0(\xi)$. It is easy to verify that Eq. (38) is a Bernoulli-type equation and its closed-form solution is:

$$\psi(\xi)=\frac{h_1(\xi)}{h_1(0)}=\frac{e^{\Gamma(\xi)}}{1-h_1(0)\int_0^{\xi}\alpha(\xi')e^{\Gamma(\xi')}\mathrm{d}\xi'} \text{ with } \Gamma(\xi)=\int_0^{\xi}\gamma(\xi')\mathrm{d}\xi' \tag{40}$$

where $h_1(0)$ is the disturbance magnitude at $\xi = 0$. For a given gradual flow depth profile $h_0(\xi)$, the behavior of $\psi(\xi)$ function (Eq. 40) describes the growth or the decay of the initial disturbance, i.e. the occurrence of unstable or stable conditions. However, owing to the non-linearity of Eq. (15), the $h_0(\xi)$ function has to be evaluated with a numerical method in a set of discrete points, and in turn the unstable character of an initial profile has to be numerically checked.

Inspection of Eq. (40) reveals that due to the non-linear term in Eq. (38) and depending on the $h_1(0)$ value, h_1 may diverge at some finite distance ξ_b from the inlet, i.e. $h_1(\xi_b)\to\infty$, and a breaking wave may occur with the formation of a shock (Witham, 1974).

Indeed, downstream to the wave breaking abscissa, the wave front technique is not more applicable and only the full numerical solution of the governing equations may allow describing the disturbance dynamics. In uniform flow, i.e. h_0=1, the α and γ coefficients (Eq. 39) assume the following constant values:

$$\alpha_N=\frac{2\lambda_N^+\mathsf{F}_N^2\left(2\beta^2-\lambda_N^+\right)-2\beta\left(\beta\mathsf{F}_N^2-1\right)+3}{2\lambda_N^+\left(\lambda_N^+-\beta\right)\mathsf{F}_N^2} \tag{41}$$

$$\gamma_N=\frac{n\left(\lambda_N^+-2\right)-1}{\lambda_N^+\left(\beta-\lambda_N^+\right)\mathsf{F}_N^2} \tag{42}$$

where:

$$\lambda_N^+=\beta+\sqrt{\beta(\beta-1)+\frac{1}{\mathsf{F}_N^2}} \tag{43}$$

In such an instance, the breaking wave distance ξ_b may be easily determined as:

$$\xi_{b,N}=\frac{1}{\gamma_N}\ln\left(1+\frac{\gamma_N}{\alpha_N}\frac{1}{h_1(0)}\right) \tag{44}$$

Under the hypothesis that the disturbance remains sufficiently small, the second-order term in Eq. (38) may be neglected and Eq. (40) simplifies into the following one:

$$\psi(\xi)=e^{\int_0^{\xi}\gamma(\xi')\mathrm{d}\xi'} \tag{45}$$

The sign of $\gamma(\xi)$ function along the initial profile $h_0(\xi)$ provides a preliminary indication about the stability to small disturbances (linear stability), as suggested for the turbulent clear-water case by Dracos and Glenne (1967). If $\gamma(\xi)$ is positive (respectively negative) along the entire initial profile, the disturbance grows (respectively decays) along the channel, and therefore the initial condition may be classified as linearly unstable (respectively stable). Conversely, if $\gamma(\xi)$ changes its sign along the channel, the evolution of small disturbances requires the numerical evaluation of Eq. (45).

Finally, in uniform conditions of flow Eq. (45) becomes:

$$\psi(\xi) = e^{\gamma_N \xi} \tag{46}$$

From Eq. (46) it follows that a uniform flow is linearly unstable whenever $\gamma_N > 0$, or equivalently whenever the Froude number exceeds the limiting value:

$$\mathsf{F}_N^* = \frac{n}{\sqrt{2n+1}} \tag{47}$$

which corresponds to the uniform marginal stability threshold deduced by Ng and Mei (1994) through normal mode analysis and by Di Cristo et al. (2013d) based on the study of the Green function.

4 Results

The results of linear and non-linear wave front analyses are separately discussed for mild and steep slope channels. Figure 3 represents the variability with the rheological index n of the uniform marginal stability Froude number expressed by Eq. (47) (Fig. 3a) and of the ratio between the critical Froude number and the uniform marginal stability one, $\mathsf{F}_{N,c}/\mathsf{F}_N^*$ (Fig. 3b). For sake of clarity, Table 1 reports the β coefficient values, the uniform marginal stability and the critical Froude numbers for different rheological indexes.

Table 1 Parameters β, F^*_N and $\mathsf{F}_{N,c}$ for different rheological index values

n	β	F^*_N	$\mathsf{F}_{N,c}$
0.1	1.04	0.09	0.978
0.2	1.08	0.17	0.963
0.5	1.14	0.35	0.935
1.0	1.20	0.58	0.912
1.5	1.23	0.75	0.901
2.0	1.25	0.89	0.894
2.5	1.26	1.02	0.899

3.0	1.27	1.13	0.886

Figure 3a indicates that F_N^* increases with n, assuming the values 0.17 for n=0.2 and 0.89 for n=2.0. Figure 3b suggests that either for a shear-thinning (n<1) or for a shear-thickening fluid, with n<2, the marginal uniform stability condition occurs in hypocritical conditions ($F_{N,c}/F_N^* > 1$). For shear-thinning fluids, unstable uniform flows may occur in both mild and steep slope channels. For shear-thickening fluids with $1 < n \leq 2$, Fig. 3b suggests that in mild slope channels the range of unstable uniform conditions is more limited. For shear-thickening fluids with $n > 2$, uniform unstable conditions are always hypercritical $\left(F_{N,c}/F_N^* < 1\right)$ and therefore they occur only in steep slope channels.

In what follows, in order to investigate the influence of gradually varying initial conditions on the stability of the base flow, for mild (respectively steep) slope channels only hypocritical, i.e. $h_0 > h_c$ (respectively hypercritical, i.e. $h_0 < h_c$) initial conditions are considered. For mild slope channels h_0>1 (respectively h_0<1) corresponds to a decelerating (accelerating) profile, while the opposite occurs in steep slope ones. The results for shear-thinning and shear-thickening fluids will be separately presented in the following two sub-sections.

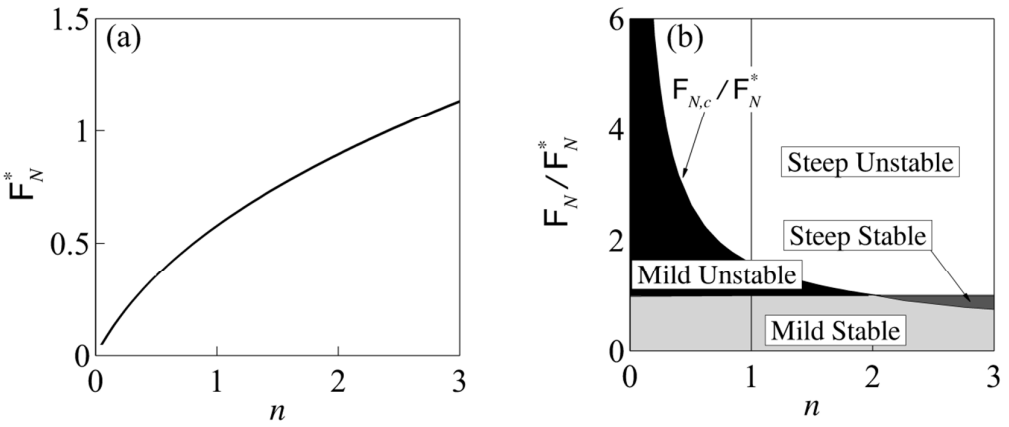

Figure 3 Uniform marginal stability Froude number (a) and the ratio of the critical and uniform marginal stability Froude numbers (b) as a function of the rheological exponent.

4.1 Shear-thinning fluids

As pointed out in the previous section the knowledge of the γ sign along an initial profile may allow to predict its linearly stable or unstable character. In Figure 4 the dependence of γ on the flow depth h_0 is shown for n = 0.2. The analysis is carried out considering mild (Fig. 4a) and steep (Fig. 4b) slope channels, separately. For the considered fluid the uniform marginal

stability Froude number value is $F_N^* = 0.17$ (Table 1) and the ratio $F_{N,c}/F_N^*$ is 5.7. In mild slope channels (Fig. 4a) stable and unstable uniform conditions are therefore both permitted. In the steep slope channel (Fig. 4b) F_N/F_N^* is always larger than 6 for the considered fluid and therefore any uniform flow is unstable. In Figure 4a (respectively Fig. 4b) the investigated flow depth range starts (respectively ends) at the critical value h_c. Having neglected the curvature effects, the free surface slope for $h_0 \approx h_c$ negatively diverges and therefore the results in the proximity of critical depth have to be taken with caution.

For both channel types, Fig. 4 clearly indicates that the linear stability of an initial profile is governed by both F_N^* and h_0 values. Similarly to Herschel & Bulkley fluids (Di Cristo et al., 2015), in mild slope channels (Fig. 4a), independently of the F_N/F_N^* ratio, $\gamma(h_0) > 0$, i.e. the linearized flow model predicts disturbance growth in a range of flow depth (h_0', h_0''). For sake of clarity, Figure 4a shows the (h_0', h_0'') pair only for the $F_N/F_N^* = 0.5$ curve. Both the lower (h_0') and the upper (h_0'') bounds of the instability range increase with the Froude number. However, while h_0' remains always below the unity (accelerating profile), the upper bound becomes larger than the uniform value whenever $F_N > F_N^*$. In steep slope channels (Fig. 4b), independently of the Froude number value, a tendency to a stabilization is expected provided that the flow depth is larger than a value $h_0''' < h_c$. The h_0''' bound increases with the Froude number.

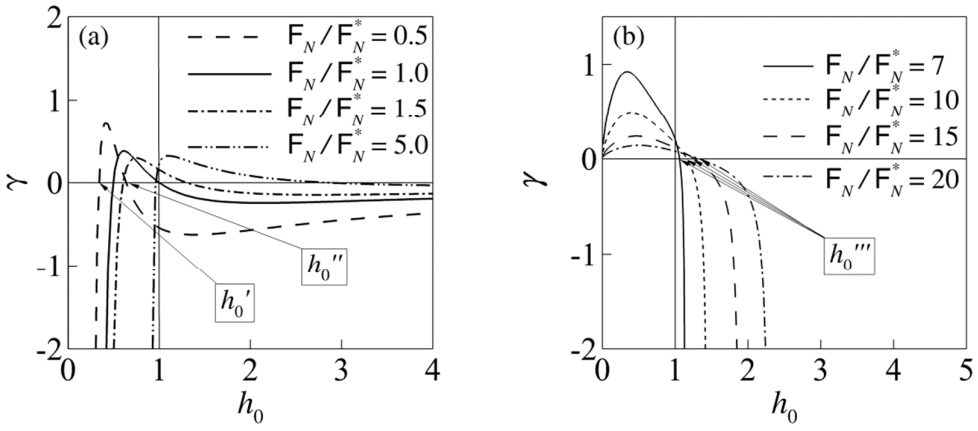

Figure 4 Dependence of the γ function on the flow depth h_0 for the shear-thinning fluid (n=0.2): (a) mild and (b) steep slope channels.

For mild slope channels, Fig. 5a depicts the dependence of both h_0' and h_0'' on the Froude number F_N, for different values of the power-law exponent, furnishing linear stability

maps. The interval (h_0', h_0'') in which linear unstable conditions may occur reduces with an increase of *n*. Figure 5b is the counterpart of Fig. 5a for steep slope channels, depicting h_0'''. Remembering that γ is negative for $h_0 > h_0'''$, Fig. 5b indicates that an increase of the rheological exponent has again a stabilizing effect, reducing the flow depth range in which linear instability may occur. The results of both Figs 4 and 5 indicate that both the initial profile and the fluid rheology influence the occurrence of instabilities of a fixed flow condition.

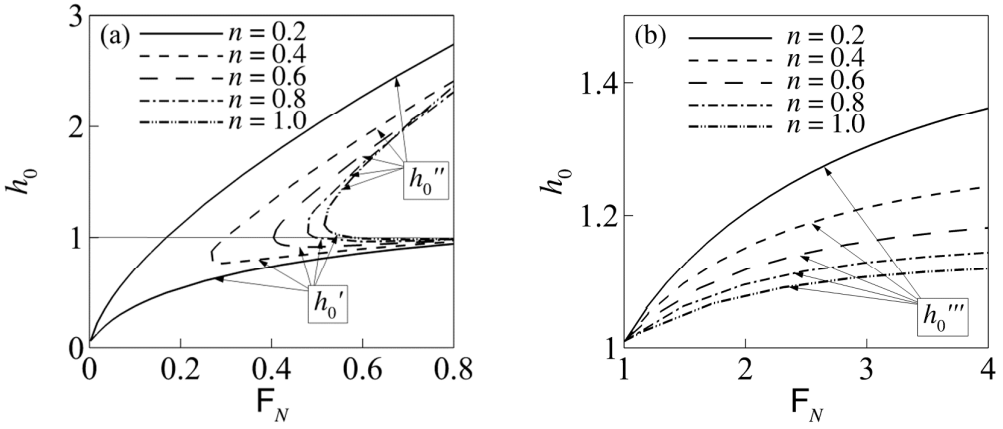

Figure 5 Linear stability maps for shear-thinning fluid: (a) mild and (b) steep slope channels.

In order to deeply investigate the effect of the initial profile on the spatial evolution of a disturbance, for the same fluid of Fig. 4 (*n*=0.2), two linearly unstable uniform flow conditions have been considered and analyzed. The first one pertains to a mild slope channel with $F_N = 1.5F_N^* = 0.25$, with $F_N = 0.26F_{N,c}$ and $h_c = 0.41$; the second one considers a steep slope channel, with $F_N = 1.69 = 10F_N^* = 1.75F_{N,c}$ and $h_c = 1.45$. For the former case, three downstream boundary conditions have been assigned, namely $h_{0,D}$ =1.0 (Uniform Profile, UP), $h_{0,D}$ =0.6 (Accelerated Profile, AP), $h_{0,D}$ =2.0 (Decelerated Profile, DP). Similarly, three upstream boundary conditions have been imposed to the steep slope case, namely $h_{0,U}$ =1.0 (Uniform Profile, UP), $h_{0,U} \cong 0.9h_c$=1.3 (Accelerated Profile, AP), $h_{0,U}$ =0.5 (Decelerated Profile, DP). The initial profiles have been determined integrating numerically Eq. (15) through a standard second-order Runge-Kutta method for a fixed dimensionless channel length of L=20 with a mesh resolution $\Delta\xi = 2 \cdot 10^{-2}$. Figures 6a and 6b represent the resulting profiles for mild and steep slope channels, respectively.

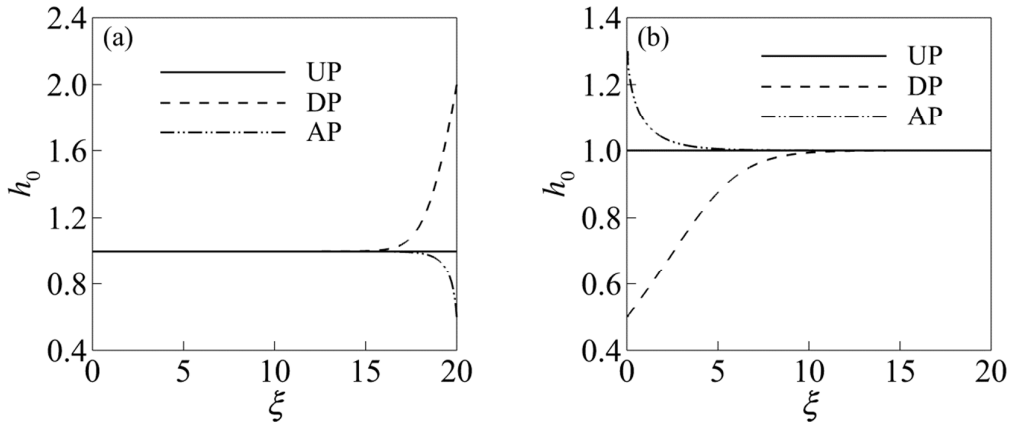

Figure 6 Initial flow depth profiles for shear-thinning fluid (n=0.2) in (a) mild and (b) steep slope channels.

For each initial profile, the spatial evolution of the perturbation has been estimated integrating Eq. (38) using the same numerical method with a perturbation imposed at the channel inlet.

For the three initial profiles in the mild slope channel, Fig. 7 shows the spatial evolution of the perturbation, obtained with three different disturbance amplitudes, namely $h_1(0)= 10^{-10}$ (Fig. 7a), representative of the linear regime, $5\cdot10^{-3}$ (Fig. 7b) and 10^{-2} (Fig. 7c) , for exploring the non-linear effects. Figure 7a shows that all profiles are linearly unstable. However, as already suggested by Fig. 4a, the decelerated initial profile induces a neat decay of the disturbance for abscissas larger than ξ~18, whereas very close to the channel outlet the accelerated one produces a slight increase of the disturbance amplitude with respect to the uniform flow case. The same behavior is illustrated by the plots of Fig. 7b. However, owing to the non-linear term in Eq. (38), in the accelerated and the uniform profiles the perturbation evolves towards a breaking wave while reaching the channel outlet, while this is not observed in the decelerated profile. With a further increase of the disturbance amplitude, Fig. 7c shows nearly coincident disturbance profiles, all with a non-linear wave breaking at the abscissa $\xi_b \sim 17$, which corresponds to the $\xi_{b,N}$ value given by Eq. (44). Such a result complies with the consideration that for $\xi \leq \xi_b$ the three initial profiles essentially overlap each other (Fig. 7a).

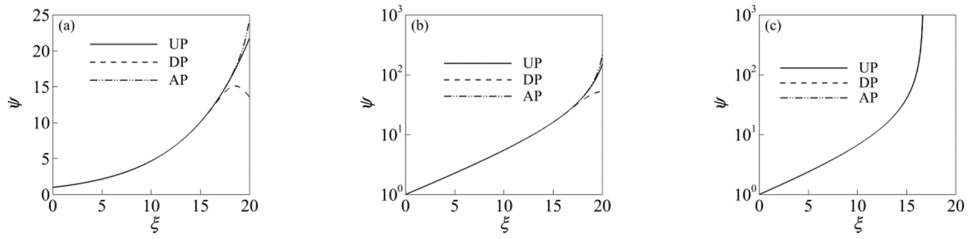

Figure 7 Disturbance evolution in terms of $\psi(\xi)$ function (Eq. 40) along the spatial abscissa ξ for shear-thinning fluid (n=0.2) in mild slope channel: (a) $h_1(0)=10^{-10}$; (b) $h_1(0)= 5\ 10^{-3}$; and (c) $h_1(0)=10^{-2}$.

As far as the steep slope channel is concerned, the disturbance spatial evolution is shown in Fig. 8. In this case, two different perturbation amplitudes have been considered, namely $h_1(0) = 10^{-10}$ (Fig. 8a) and $h_1(0) = 10^{-2}$ (Fig. 8b), for exploring both linear and non-linear regimes.

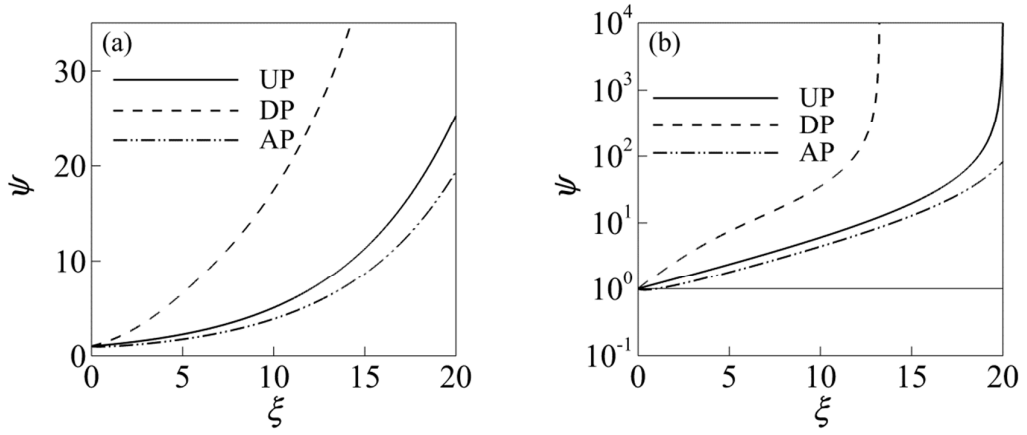

Figure 8 Disturbance evolution in terms of $\psi(\xi)$ function (Eq. 40) along the spatial abscissa ξ for the shear-thinning fluid (n=0.2) in steep slope channel: (a) $h_1(0)=10^{-10}$; and (b) $h_1(0)=10^{-2}$.

Figures 8a and 8b indicate that for all profiles the disturbance magnitude increases with ξ, with the growth rate of the accelerated (respectively decelerated) profile smaller (respectively larger) than the uniform one, as suggested by the γ function behavior (Fig. 4b). In the linear regime (Fig. 8a) no wave breaking is observed within the considered channel length. When the non-linear terms are triggered (Fig. 8b), wave breaks in both uniform (ξ_b~ 20) and decelerated (ξ_b~13) profiles, while this is not observed in the accelerated one, within the considered channel length.

4.2 Shear-thickening fluids

The counterpart of Fig. 4 for a shear-thickening fluid (n=1.5) for both mild and steep slope channels is represented by Fig. 9. For such a fluid $F_N^* = 0.75$ and the ratio between the critical Froude number $F_{N,c}$ and the stability limit F_N^* is 1.2. Therefore the uniform flows in steep slope channels are always linearly unstable. In mild slope case, both stable and unstable

conditions may occur, although the range of Froude numbers in which unstable conditions are found is very narrow, as suggested by Fig. 3b. Also in this case, in Figure 9a (respectively Fig. 9b) the flow depth range starts (respectively ends) at the critical value for the mild (respectively steep) slope channel.

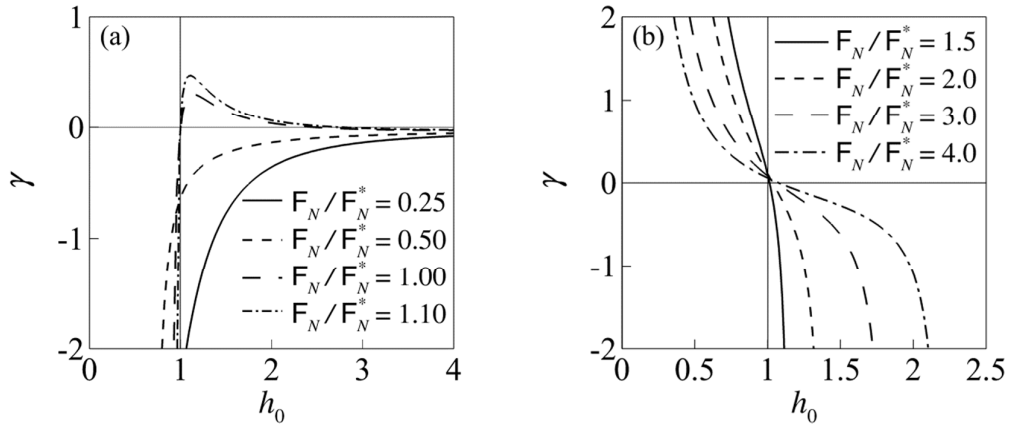

Figure 9 Dependence of the γ function on the flow depth h_0 for shear-thickening fluid (n=1.5): (a) mild and (b) steep slope channels.

As far as mild slope channels are concerned, differently from the shear-thinning fluid, Fig. 9a indicates that for $F_N < F_N^*$ the flow is linearly stable for any depth. On the other hand, similarly to the shear-thinning fluid for $F_N \geq F_N^*$ there exists a flow depth range $\left(h_0', h_0''\right)$ in which $\gamma > 0$. Therefore, as well as the n<1 case, a tail-water boundary condition inducing a decelerated profile with $h_{0,D} > h_0''$ could exert a stabilizing effect. Conversely, the linear instability cannot be promoted by an accelerating initial profile.

In the steep slope case (Fig. 9b), similarly to the shear-thinning fluid, the instability region is upper-bounded by the flow depth $h_0''' < h_c$, while γ<0 for $h_0 > h_0'''$. Then, the tendency to a stabilization is expected for accelerating profiles. However, differently from the shear-thinning case, the γ function diverges for $h_0 \to 0$, implying an unbounded disturbance growth. Such a different behavior between shear-thinning and shear-thickening fluids is essentially due to the asymptotic behavior of the profile slope for vanishing h_0 (see Figs. 2a and 2c).

In Fig. 10, for different values of the power-law exponent, the dependence of the $\left(h_0', h_0''\right)$ pair (Fig. 10a) and of the h_0''' value (Fig. 10b) on the Froude number F_N is depicted, for mild and steep slope channels, respectively. Figure 10a suggests that while the lower bound h_0' slightly depends on the power-law exponent and the Froude number, the upper

bound h_0'' strongly increases with n and with F_N. The lower bound h_0' is always larger than unity (uniform depth) and therefore an accelerating initial profile is not linearly destabilizing, independently of the n value. Conversely, as far as the steep slope channel is concerned, Fig. 10b indicates that the h_0''' value decreases with n similarly to the shear-thinning fluid, although in a smaller range.

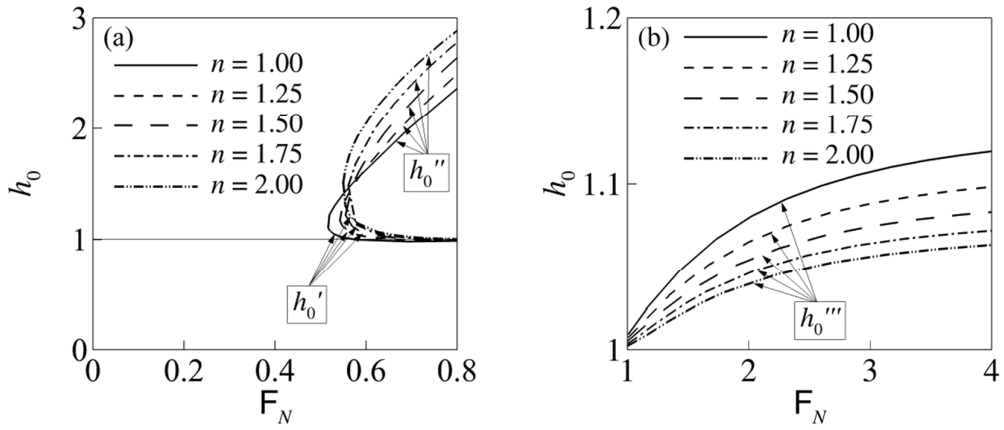

Figure 10 Linear stability maps for shear-thickening fluid: (a) mild and (b) steep slope channels.

Since for shear-thickening fluids in mild slope channels, the range of Froude numbers corresponding to linearly unstable conditions is extremely narrow (see also Fig. 3b), the spatial evolution of the perturbation is analyzed only with reference to steep slope channels. To this aim, the same fluid of Fig. 9 has been considered (n=1.5) and the Froude number has been set equal to $F_N = 4F_N^* = 3$ ($h_c = 2.23$). Two upstream boundary conditions have been considered, i.e. $h_{0,U} \cong 0.9h_c = 2.0$ (Accelerated Profile, AP) and $h_{0,U} = 0.5$ (Decelerated Profile, DP), along with the uniform one (UP: $h_{0,U} = 1.0$). The initial flow profiles, represented in Fig. 11a, follow from the numerical solution of Eq. (15), also in this case evaluated over a dimensionless channel length $L = 20$ with mesh spacing $\Delta\xi = 2 \cdot 10^{-2}$. In addition, for the sake of comparison, the Newtonian case has been considered, assuming $F_N = 4F_N^* = 2.3$ $\left(h_c = 1.86\right)$. As far as the decelerated profile is concerned, the boundary condition $h_{0,U}$ has been fixed equal to 0.5, while for the accelerated one the value $h_{0,U} \cong 0.9h_c = 1.7$ has been considered. Figure 11b reports the computed profiles.

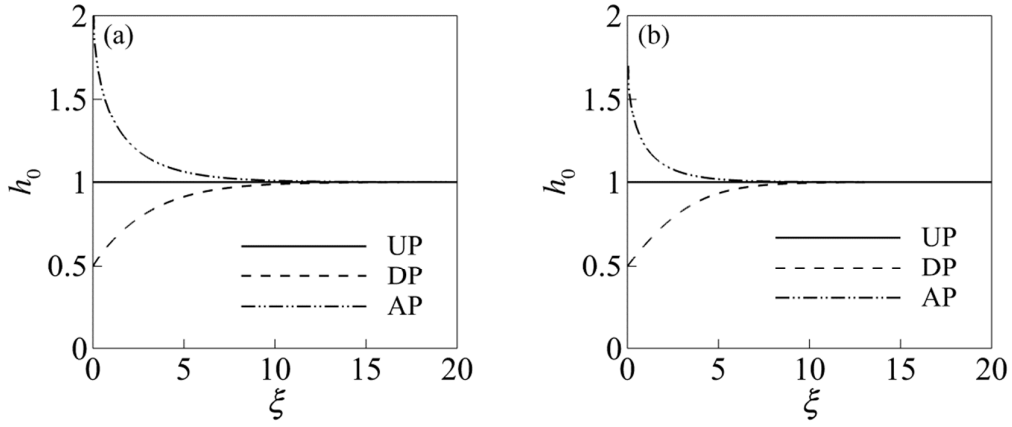

Figure 11 Initial flow depth profiles in steep slope channel. (a) Shear-thickening fluid (n=1.5); (b) Newtonian fluid (n=1).

Two different perturbation amplitudes have been considered, namely $h_1(0) = 10^{-10}$ and $h_1(0) = 10^{-2}$ again in order to explore both linear and non-linear conditions. The spatial evolution of the disturbances is represented in Figs. 12a and 12b for $h_1(0) = 10^{-10}$ and $h_1(0) = 10^{-2}$, respectively, for the shear-thickening fluid. The counterpart of Fig. 12 for the Newtonian fluid is Fig. 13.

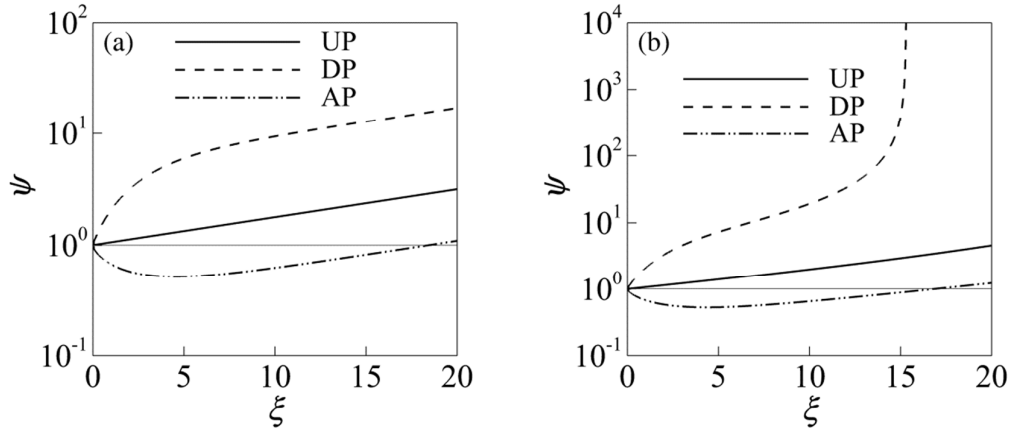

Figure 12 Disturbance evolution in terms of $\psi(\xi)$ function (Eq. 40) along the spatial abscissa ξ for shear-thickening fluid (n=1.5) in steep slope channel: (a) $h_1(0) = 10^{-10}$; (b) $h_1(0) = 10^{-2}$.

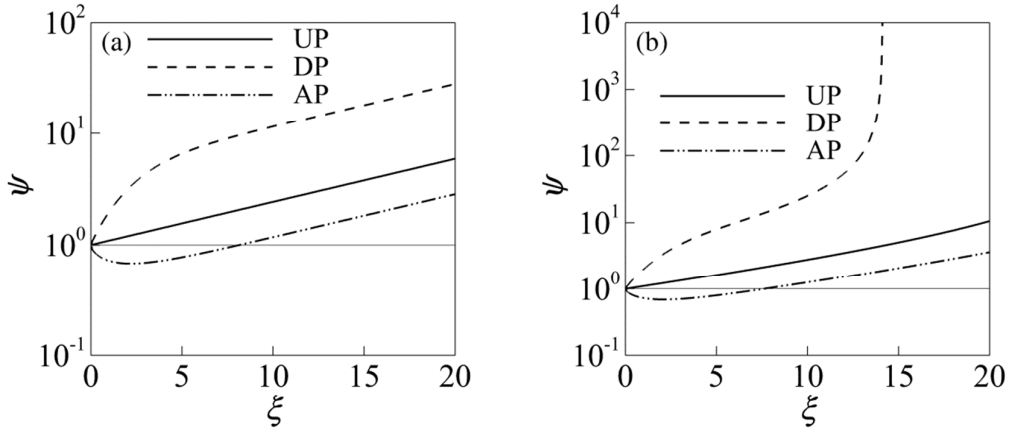

Figure 13 Disturbance evolution in terms of $\psi(\xi)$ function (Eq. 40) along the spatial abscissa ξ for Newtonian fluid (n=1) in steep slope channel: (a) $h_1(0) = 10^{-10}$; (b) $h_1(0) = 10^{-2}$.

As far as the linear case is concerned, Fig. 12a shows an exponential disturbance growth on the uniform initial profile, without wave breaking within the considered channel length. In both accelerated and decelerated cases, the initial free-surface profile induces considerable differences in the growth-rate values close to the inlet, i.e. for $\xi \leq 10$. According to the $\gamma(\xi)$ function behavior (Fig. 9b), the decelerated (respectively accelerated) profile shows a larger (respectively smaller) disturbance growth-rate compared to the uniform one. For the accelerated profile, owing to the negative sign of $\gamma(\xi)$ in the first part of the channel (Fig. 9b), the disturbance magnitude reduces, i.e. $\psi < 1$, then a successive increase along the channel follows. For $\xi > 10$ the disturbance growth-rate is essentially independent of the initial profile. In fact for $\xi > 10$ the flow profile, either in the accelerating or in the decelerating case, closely approaches the uniform condition (Fig. 11a). The non-linear effects (Fig. 12b) do not alter the qualitative spatial evolution of the disturbance over the uniform and the accelerated profiles, even if a quantitative increase of the disturbance amplitude is detected. In the decelerated profile, the non-linearity induces a breaking wave at $\xi_b \approx 15$, significantly upstream compared with the corresponding value computed in uniform condition $\xi_{b,N} \approx 37$ from Eq. (44). As far as the accelerated profile is concerned, the wave breaking point does not occur in the considered channel length. Therefore, similarly to the shear thinning case, the initial profile may shift downstream or upstream the roll-waves development dependently on the free-surface profile.

From the qualitative point of view, the results for the Newtonian fluid (Fig. 13) strongly resemble those of the shear-thickening fluid, with minor quantitative differences. Indeed, independently of the amplitude of the disturbance, the shear-thickening behavior amplifies the portion of the channel in which the ψ function is smaller than one. Conversely,

for the decelerated profile, the breaking wave occurs closer to channel inlet in the Newtonian case than in the shear-thickening one.

The above results jointly indicate that in a power-law shear-thinning fluid flowing in a mild slope channel, independently of the Froude number of the uniform flow, a decelerated initial profile reduces the disturbance spatial growth compared with the uniform condition, while for an accelerated profile the opposite is found. Only the former feature has been detected for shear-thickening fluids. Conversely, in a steep slope channel, independently of the *n* value, an acceleration of the profile induces a smaller disturbance growth compared with the uniform one whereas a deceleration enhances it. To confirm the above conclusions, in the next section the results of fully non-linear simulations are reported.

5 Fully non-linear analysis

In order to confirm the influence of the steady initial profile on the disturbance growth-rate, the spatio-temporal evolution of a flow depth perturbation has been analyzed through the solution of the full non-linear problem expressed by the system (7)-(8), written in its conservative form. To this aim, a finite-volume numerical method has been employed. The associated Riemann problem, i.e. the evaluation of convective fluxes on interfaces of finite-volumes, is handled with the second order Runge-Kutta-TVD scheme (Gottlieb & Shu, 1998; Harten, 1983). A concise description of the adopted numerical method is reported in the Appendix. At the channel inlet, the following Gaussian perturbation is imposed on the discharge:

$$D(t) = \delta \mathrm{e}^{-\varepsilon\left(t-t_p\right)^2} \tag{48}$$

where δ, t_p and ε are the perturbation parameters. To effectively simulate the disturbances leaving the channel outlet without spurious reflections, even in presence of hypocritical flow condition, i.e.: for $\lambda^- < 0$, a non-reflecting boundary condition is required. Herein the local absorbent boundary condition technique proposed by Paz, Storti and Garelli (2011) has been applied. Some details of this technique are provided in the Appendix. All simulations have been carried out discretizing the domain into 50000 volumes of equal size with a CFL number based on λ^+ order of 10^{-2}. For clear-water roll-waves simulations, the results by Bohorquez and Rentschler (2011) demonstrated that under these conditions the second-order method performs comparably well to a more involved fifth-order WENO.

To assess at the full non-linear level the effect of the initial condition, the same initial flow profiles discussed in the previous section have been considered, along with the same shear-thinning and shear-thickening fluids. The perturbation parameters have been chosen as $\delta = 5 \cdot 10^{-2}$, $t_p = 1$ and $\varepsilon = 10$ (100 for the shear-thinning mild slope channel), in order to suitably trigger the non-linearity of the flow model.

Figure 14 represents the space-time evolution of the nonlinear disturbance h-h_0 for the three considered initial conditions depicted in Fig. 6a for the shear-thinning fluid in mild slope channel. Three instantaneous flow profiles at t= 1.5, 3, 4.7 are compared. Owing to the non-linearity, in all the considered profiles the smooth flow disturbance evolves into a downstream-propagating shock, whose shape clearly resembles roll-waves. A negative depression wave is also always observed upstream the shock. Even if the perturbation evolution is qualitatively similar, the accelerated profile produces a slightly increased growth of the disturbance respect to the uniform flow solution. Differently, the decelerated profile has a more significant effect on the wave evolution, with a sensible reduction in the disturbance growth, along with a celerity increase (see the close-up box of Fig. 14).

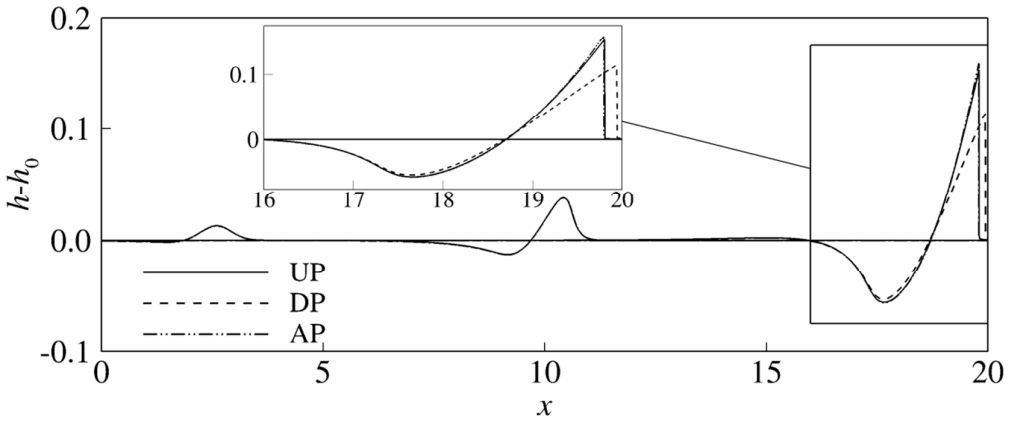

Figure 14 Disturbance spatial evolution for shear-thinning fluid (n=0.2) in mild slope channel. Flow profiles at t = 1.5, 3, 4.7.

For the same rheology, the steep slope initial profiles of Fig. 6b have been also considered. Figure 15 compares the evolution of the disturbance in these three initial profiles at t= 5, 7.5, 10. The results reveal an even more appreciable effect of the initial condition than in the mild slope case, with a noticeable change in both wave shape and migration speed. The perturbation in the uniform flow is characterized by a downstream front progressively steepening and evolving into a bore, with positive amplitude growing in time. On the upstream tail of the perturbation a depression wave is detected, with its negative height progressively increasing in time too. In the accelerated initial profile case the behavior is qualitatively similar, but with a smaller perturbation growth-rate and celerity respect to uniform case. On the other hand, the decelerated initial profile strongly promotes the growth of the perturbation amplitude and the wave celerity. It is also observed that a further shock

develops on the upstream tail of the perturbation with the formation of a second smaller bump lagging behind the main one.

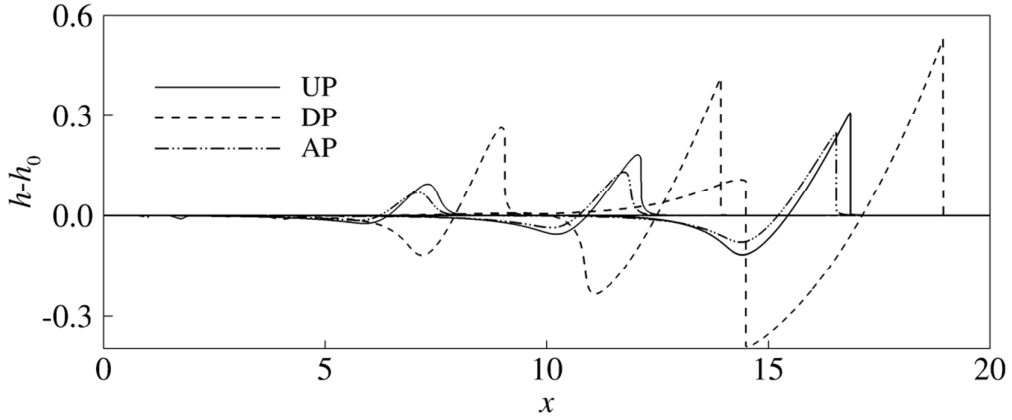

Figure 15 Disturbance spatial evolution for shear-thinning fluid (n=0.2) in steep slope channel. Flow profiles at t = 5, 7.5, 10.

Finally Fig. 16 reports the space-time evolution of the perturbation in the shear-thickening fluid in steep slope channel for the initial conditions of Fig. 11a, depicting the same instantaneous profiles of Fig. 15 (t= 5, 7.5, 10). It is easily to recognize that the accelerated initial profile has a stabilizing effect, which inhibits the disturbance to develop into a shock within the considered channel length, with also an appreciable reduction of its migration speed. At the opposite, the decelerated initial condition produces an increase of both the growth and the migration velocity of the perturbation, promoting the development of a discontinuous roll-wave-like disturbance.

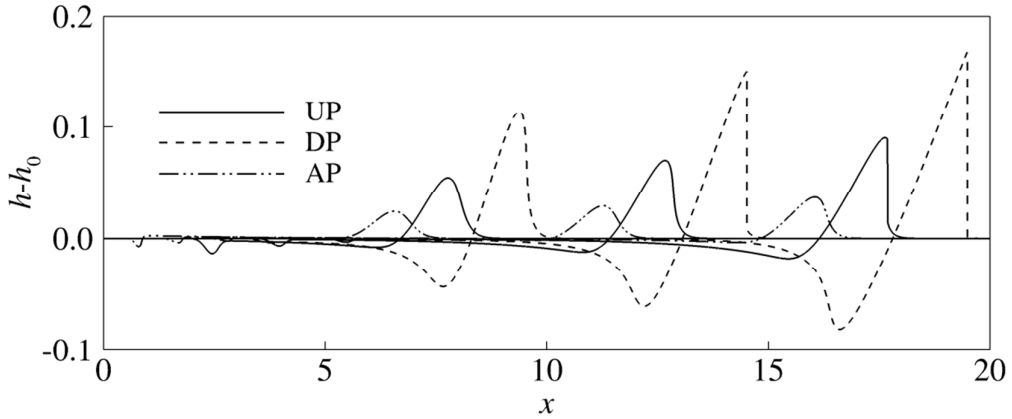

Figure 16 Disturbance spatial evolution for shear-thickening fluid (n=1.5) in steep slope channel. Flow profiles at t = 5, 7.5, 10.

For sake of comparison, the same simulation has been carried out also for Newtonian fluid (n=1) and Fig. 17 reports the space-time evolution of the perturbation, considering the initial flow profiles depicted in Fig. 11b. As noted for the near-front expansion analysis, the qualitative behavior is similar to the shear-thickening case. A closer investigation reveals that the Newtonian fluid undergoes a slightly more pronounced growth for any of the three initial conditions, consistently with the results found with the near-front expansion analysis.

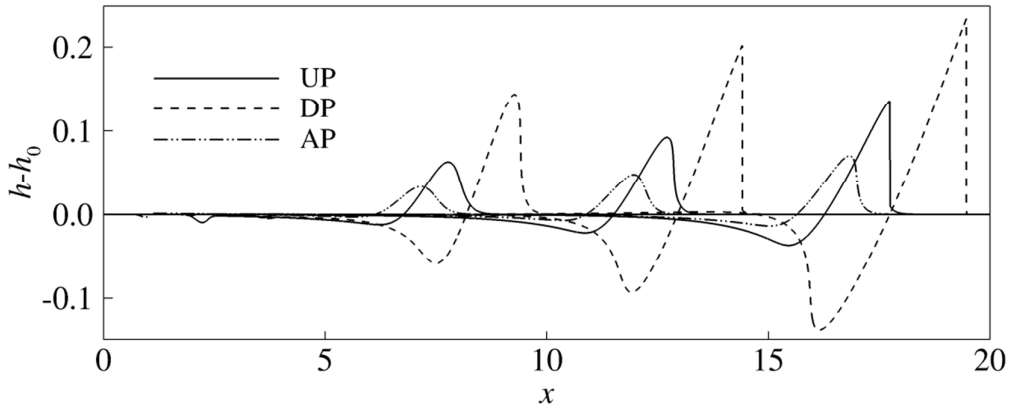

Figure 17 Disturbance spatial evolution for Newtonian fluid (n=1) in steep slope channel. Flow profiles at t = 5, 7.5, 10.

In conclusion, the results of the full non-linear simulations demonstrate a strong effect of the initial profile on the disturbance evolution, influencing its growth-rate and celerity. Substantial differences are found in mild and steep slope channels. The results of the near-front expansion analysis confirm the stabilizing (respectively destabilizing) effect of an initially decelerated (respectively accelerated) profile for a shear-thinning fluid in a mild slope channel. On the contrary, in a steep slope channel, independently of the shear-thinning or shear-thickening behavior of the flowing medium, an initially decelerated profile enhances the instability of the flow profile up to the formation of finite non-linear perturbations with roll-wave shape. Finally, the full non-linear analysis shows that independently of the fluid rheology, in mild slope channel the increase of disturbance growth-rate slows down the perturbation migration, whereas the opposite occurs in steep slope channels.

Well-documented experiments may provide the definitive confirmation of the present theoretical results. In the following, a preliminary design of the experimental conditions is provided, addressing both the rheological properties of the fluids and the flow conditions

considered in the theoretical analysis. As a suitable shear-thinning fluid, a kaolinite suspension with a volume concentration of about 10%, with typical values of n=0.2, ρ = 1200 kgm^{-3} and μ_n=1.4 Pa s^n ($F_N^* = 0.17$, $F_{N,c} = 0.96$) has been considered for the experiment design (Ng & Mei, 1994). The shear-thickening fluid may be prepared with a mixture of water and cornstarch according to Longo et al. (2015), resulting in the following rheological parameters: n=1.5, ρ = 1220 kgm^{-3} and μ_n=0.4 Pa s^n ($F_N^* = 0.75$, $F_{N,c} = 0.90$). With these two fluids, the shear-thinning flow conditions herein investigated could be reproduced in a tiltable laboratory flume 35 m long, 0.8 m wide. A flume length of 3 m is sufficient for the shear-thickening case. Table 2 reports the data for a set of possible experimental tests, i.e. the channel slope and the dimensional flow rate for unit width, along with the corresponding dimensional uniform and critical flow depths and the Froude number.

Table 2 Design data for experiments

Test	$\sin\theta$	$\tilde{q}_N$(m^{2}s^{-1})	$\tilde{h}_N$(m)	$\tilde{h}_c$(m)	F_N/F^*_N
1 – shear-thinning, mild slope	0.012	0.002	0.021	0.008	1.5
2 – shear-thinning, steep slope	0.02	0.019	0.024	0.035	10.0
3 – shear-thickening, steep slope	0.40	0.173	0.072	0.160	4.0

Different initial profiles in both steep and mild slope channels may be obtained by properly operating with a gate at the inlet or at the outlet of the flume.

6 Conclusions

In the paper the spatial evolution of a disturbance superposed to non-uniform flows of a power-law fluid has been studied, in order to investigate the effect of initial gradually varied profiles on the roll-waves development. The considered flow model is based on the von Kàrmàn's integral method, which allows capturing the physics of the process without increasing the mathematical complexity. The study is carried out combining theoretical and numerical approaches to track the evolution of the initial disturbance. The former approach has been developed using the nonlinear near-front expansion technique, which reproduces the results of linear stability analysis in the limit of small perturbation magnitude. This technique exploits the hyperbolic character of the considered flow model to follow the evolution of an initial perturbation in a moving reference frame. The numerical analysis has been carried out through a Finite Volume second-order Runge-Kutta TVD scheme. A generalization for power-law fluids of the locally adsorbing boundary conditions, originally proposed for clear-water shallow water equations, has been provided. Both the approaches concur to state that for both shear-thinning and -thickening fluids non-uniform initial conditions strongly

influence the disturbance space-time evolution, affecting consequently the conditions in which instabilities occur.

For shear-thinning fluids, for which uniform linearly unstable conditions occur in both mild and steep slope channels, a different influence of the initial profile has been found dependently on the channel slope. Indeed, accelerated profiles promote the disturbance growth, compared with the uniform condition, in mild slope channels and inhibit it in steep slope ones. An opposite behavior has been found for the decelerated profiles, which reduce the spatial growth of the disturbance in the mild slope channel and enhance it in steep slope channel. Moreover, as far as the mild slope channel is concerned, while the accelerated profile does not substantially modify the perturbation celerity, with respect to the uniform condition, the decelerated one increases it. In presence of steep slope channels, the dependence of the perturbation celerity on the initial profile is visible in both accelerated and decelerated profiles. Indeed in the former (respectively latter) case the celerity is smaller (respectively larger) than the corresponding one in uniform condition.

For shear-thickening fluids, while in steep slope channels the same behavior of shear-thinning ones is observed in terms of both spatial growth and celerity of the perturbation, in mild slope channels only the stabilizing attitude of a decelerated initial profile has been found.

Although accurate experiments are needed for a definitive confirmation, present theoretical results indicate that the analyses assuming uniform condition, instead of the actual initial gradually varying profile, may lead to overestimate or underestimate the growth rate of the disturbance and therefore the spatial roll-waves prediction. Such a conclusion has to be accounted for in formulating predictive criteria for the occurrence of roll waves in mud flow based on the channel length. Moreover, the influence of the initial condition on the stability suggests the adoption of proper boundary conditions as a passive way to control the roll-waves development, either for inhibiting or for promoting their occurrence. The former action is of interest in environmental engineering while the latter may improve the performance of industrial processes.

Funding

This work was partly supported by Regione Campania [grant LR5/02-2008 n° B36D14000770002].

Appendix. Numerical method

The numerical solution of system (7)-(8) is sought for starting from the corresponding conservative form:

$$\frac{\partial \mathbf{w}}{\partial t}+\frac{\partial \mathbf{F}(\mathbf{w})}{\partial x}=\mathbf{P}(\mathbf{w}) \tag{A.1}$$

where:

$$\mathbf{w}=\begin{bmatrix} h \\ hu \end{bmatrix},\ \ \mathbf{F}(\mathbf{w})=\begin{bmatrix} hu \\ \beta hu^2+\frac{1}{2}\frac{h^2}{\mathsf{F}_N^2} \end{bmatrix},\ \ \mathbf{P}(\mathbf{w})=\begin{bmatrix} 0 \\ \frac{\tau_b-h}{\mathsf{F}_N^2} \end{bmatrix} \tag{A.2}$$

which have been discretised by a conventional Finite-Volume approach:

$$\frac{\partial \mathbf{W}}{\partial t}+\frac{1}{\Delta x}\left(\mathbf{F}^*_{i+1/2}-\mathbf{F}^*_{i-1/2}\right)=\mathbf{P}^* \tag{A.3}$$

where Δx is the space interval, $\mathbf{W}$ denotes the average value of the conserved variable in the volume, $\mathbf{F}^*$ is a properly defined numerical approximation of the flux at the volume interfaces, and $\mathbf{P}^*$ is the volume-averaged value of the source term. In the present numerical method, the Harten-Lax-Van Leer (HLL) scheme (Harten, 1983), is adopted for the evaluation of the interface numerical flux:

$$\mathbf{F}^*=\begin{cases} \mathbf{F}^L & \text{if } 0\le\lambda^L \\ \dfrac{\lambda^R\mathbf{F}^L-\lambda^L\mathbf{F}^R+\lambda^R\lambda^L\left(\mathbf{w}^R-\mathbf{w}^L\right)}{\lambda^R-\lambda^L} & \text{if } \lambda^R\le 0\le\lambda^L \\ \mathbf{F}^R & \text{if } 0\ge\lambda^R \end{cases} \tag{A.4}$$

with:

$$\lambda^R=\max_{R,L}\left(\lambda^+\right),\ \lambda^L=\min_{R,L}\left(\lambda^-\right) \tag{A.5}$$

The HLL schemes operates on the values of the conserved variables at the two sides of the interface, $\mathbf{w}^L$ and $\mathbf{w}^R$, that are in turn estimated by a piecewise linear reconstruction limited by the minmod operator (Gottlieb & Shu, 1998). The volume-averaged source term $\mathbf{P}^*$ is evaluated based on pointwise approximation. The time integration is performed according to the two-step Runge-Kutta scheme proposed by Gottlieb and Shu (1998):

$$\frac{\partial \mathbf{W}}{\partial t}+=\mathbf{P}^*-\frac{1}{\Delta x}\left(\mathbf{F}^*_{i+1/2}-\mathbf{F}^*_{i-1/2}\right)=\mathbf{T}(\mathbf{W}) \tag{A.6}$$

with:

$$\begin{aligned} \mathbf{W}^{(1)}&=\mathbf{W}^n+\Delta t\mathbf{T}\left(\mathbf{W}^n\right) \\ \mathbf{W}^{n+1}&=\frac{1}{2}\mathbf{W}^n+\frac{1}{2}\mathbf{W}^{(1)}+\frac{1}{2}\Delta t\mathbf{T}\left(\mathbf{W}^{(1)}\right) \end{aligned} \tag{A.7}$$

A locally adsorbing boundary condition is required at the outlet. In clear-water shallow flows, a customary implementation of this condition consists in enforcing a constant

value of the Riemann Invariants of the governing equations. Unfortunately, for the PDEs system (7)-(8) the closed form expression of Riemann Invariants is not readily available. To overcome this difficulty, the method proposed by Paz et al. (2011) has been adopted. The Authors show that for a diagonalised linear PDE system, boundary conditions have to be prescribed on the characteristic components **V** according to the sign of the characteristic celerities at the boundaries. This can be expressed in a compact mathematical form through the Projection Matrices in the space of the characteristic components **V**:

$$\begin{aligned} \mathbf{\Pi}_V^+\left(\mathbf{V}-\mathbf{V}_\mathrm{U}\right)&=0 \text{ at } x=0 \\ \mathbf{\Pi}_V^-\left(\mathbf{V}-\mathbf{V}_\mathrm{D}\right)&=0 \text{ at } x=L \end{aligned} \tag{A.8}$$

where $\mathbf{V}_\mathrm{U}$ and $\mathbf{V}_\mathrm{D}$ denote the prescribed states at the two boundaries and the two Projection Matrices read:

$$\begin{aligned} \mathbf{\Pi}_{V,jk}^+ &= \begin{cases} 1 & \text{if } j=k \text{ and } \lambda^+>0 \\ 0 & \text{otherwise} \end{cases} \\ \mathbf{\Pi}_{V,jk}^- &= \begin{cases} 1 & \text{if } j=k \text{ and } \lambda^-<0 \\ 0 & \text{otherwise} \end{cases} \end{aligned} \tag{A.9}$$

The expression of the projection matrices in the primitive variables **u** easily follows from the change of basis $\mathbf{\Pi}_u^\pm = \mathbf{Q}\mathbf{\Pi}_V^\pm\mathbf{Q}^{-1}$ where **Q** denotes the matrix which diagonalizes the original linear system.

Since the problem is non-linear the flux Jacobian **A** in Eq. (7) and the projection matrices $\mathbf{\Pi}_u^\pm$ in Eq. (A.9) depend on the flow variables. It may be however assumed that the flow is composed of small perturbations around a reference state, according to which the projection matrix can be computed. Following the ULSAR strategy proposed by Paz et al. (2011), the previous state is assumed as the reference one. The transmissive outlet boundary condition is therefore described by the following linear system:

$$\mathbf{\Pi}_u^-\left(\mathbf{u}^t\right)\left(\mathbf{u}^{t+\Delta t}-\mathbf{u}^t\right)=0 \tag{A.10}$$

which matrix can be expressed as:

$$\mathbf{\Pi}_u^\pm(\mathbf{u})=\begin{bmatrix} \frac{1}{2}\left[1\pm\frac{u\mathsf{F}_N(\beta-1)}{\sqrt{(u\mathsf{F}_N)^2\beta(\beta-1)+h}}\right] & \pm\frac{1}{2}\frac{(u\mathsf{F}_N)^2\beta(\beta-1)+h}{hF_N\sqrt{(u\mathsf{F}_N)^2\beta(\beta-1)+h}} \\ \mp\frac{hF_N}{2}\frac{\left[u\mathsf{F}_N(\beta-1)\right]^2-\left[(u\mathsf{F}_N)^2\beta(\beta-1)+h\right]}{\left[(u\mathsf{F}_N)^2\beta(\beta-1)+h\right]^{3/2}} & \frac{1}{2}\left[1\mp\frac{u\mathsf{F}_N(\beta-1)}{\sqrt{(u\mathsf{F}_N)^2\beta(\beta-1)+h}}\right] \end{bmatrix} \tag{A.11}$$

To show the effectiveness of the present approach, Fig. A.1 plots the solution of the shear-thinning fluid in mild slope channel discussed in Section 5 (uniform initial condition)

starting from t = 4.7 (last time step of Fig. 14) and with subsequent time levels shifted of 0.0625. The considered time window corresponds to the developed perturbation leaving the computational domain through the channel outlet under hypocritical conditions. It is noted that the shock-wave impinging the downstream end does not exhibit any spurious reflection despite the hypocritical regime and the strong unsteadiness of the flow.

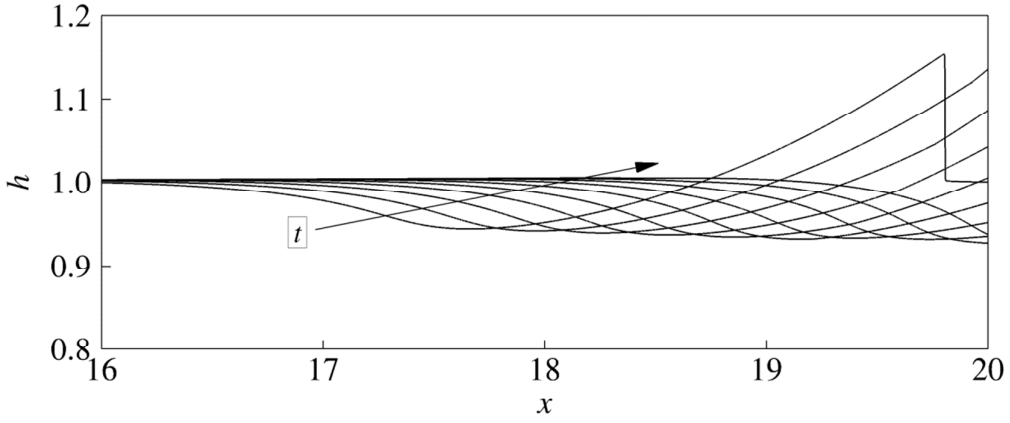

Figure A.1 Disturbance spatial evolution for shear-thinning fluid (n=0.2) in mild slope channel. Flow profiles from t = 4.7 every 0.0625.

The matrix operator defined in Eq. (A.11) may be usefully employed to model the free-surface power-law flow problem when a change of flow regime dynamically takes place. The change of regime is problematic from several points of view. For instance, the assignment of non-reflecting boundary conditions at a fictitious outlet allows saving computational resources, truncating the real unbounded domain. Moreover, the boundary conditions herein provided for a power-law fluid may automatically account for the change of Jacobians structure, when the flow regime changes from hypocritical to hypocritical or vice-versa.

Notation

A = coefficient matrix (-)

D = Gaussian perturbation (-)

$\mathbf{e}^{\pm}$ = left eigenvectors of the **A** matrix (-)

F = Flux vector (-)

$\mathbf{F}^{*}$ = Numerical Flux vector (-)

$f_1, f_2, f_3, f_4,$ = dimensionless coefficients (-)

F_N = Froude number with reference to the uniform condition (-)

F_N^* = Froude number in marginal stability condition (-)

g = gravity acceleration (ms^{-2})

h = dimensionless flow depth (-)

$h_0^{'}$, $h_0^{''}$ = lower and upper bounds of the instability range in a mild slope channel (-)

$h_0^{'''}$ = upper bound of the instability range in a steep slope channel (-)

I = identity matrix (-)

L = dimensionless channel length (-)

$\widetilde{l}_N$ = reference length scale (m)

n = exponent of the power-law fluid (-)

P = source term vector (-)

$\mathbf{P}^*$ = volume-averaged value of the source term (-)

Q = diagonalizing matrix (-)

$\widetilde{q}_N$ = unit discharge (m^2s^{-1})

s = source vector (-)

t = dimensionless time (-)

u = dimensionless depth-integrated streamwise velocity(-)

u , w = primitive and conservative variables vector

V = characteristic components vector (-)

W = cell-averaged conservative variables vector (-)

$\mathbf{w}^L$, $\mathbf{w}^R$ = conserved variables at the two sides of the interface (-)

x = dimensionless streamwise coordinate (-)

α = dimensionless function (-)

β = momentum correction factor (-)

γ = dimensionless function (-)

δ = perturbation parameter (-)

$\Delta\xi$, Δx = mesh spacing resolution (-)

ε = perturbation parameter (-)

ξ, η = transformed variables (-)

θ = angle of bottom slope (rad)

$\lambda^{\pm}$ = eigenvalues of **A** (-)

λ^L , λ^R = minimum characteristic slopes at the two sides of a cell interface (-)

μ_n = consistency of the power-law fluid (Pa s^n)

$\mathbf{\Pi}_u^{\pm}$, $\mathbf{\Pi}_V^{\pm}$ = projection matrices (-)

ρ = fluid density (kgm^{-3})

τ_b = dimensionless bottom stress (-)

ψ = perturbation amplitude ratio (-)

Subscript

0	steady state conditions
1	perturbed conditions at the first order
2	perturbed conditions at the second order
N	normal flow conditions
D	downstream channel section (outlet)
U	upstream channel section (inlet)
b	breaking wave point
c	critical condition

Superscript

~	dimensional quantities

References

Ancey, C. (2007). Plasticity and geophysical flows. A review. *Journal of Non-Newtonian Fluid Mechanics*, 142, 4–35. doi:10.1016/j.jnnfm.2006.05.005.

Bagnold, R.A. (1954). Experiments on a gravity-free dispersion of large solid spheres in a Newtonian fluid under shear, *Proceedings of the Royal Society of London A,* 225, 49–63. doi: 10.1098/rspa.1954.0186

Balmforth, N.J., & Craster, R.V. (1999). A consistent thin-layer theory for Bingham plastics. *Journal of Non-Newtonian Fluid Mechanics*, 84(1), 65–81. doi:10.1016/S0377-0257(98)00133-5

Balmforth, N.J, & Liu, J.J. (2004). Roll waves in mud. *Journal of Fluid Mechanics*, 519, 33–54. doi:10.1017/s0022112004000801

Bohorquez, P. (2010). Competition between kinematic and dynamic waves in floods on steep slopes. *Journal of Fluid Mechanics*, 645, 375–409. doi:10.1017/s002211200999276x

Bohorquez, P., & Rentschler, M. (2011). Hydrodynamic instabilities in well-balanced finite volume schemes for frictional shallow water equations. The kinematic wave case. *Journal of Scientific Computing*, 48 (1-3), 3–15. doi:10.1007/s10915-010-9444-4

Bouchut, F., & Boyaval, S. (2013). A new model for shallow viscoelastic fluids. *Mathematical Models and Methods in Applied Scences.*, 23, 1479–1526. doi:10.1142/s0218202513500140

Bouchut, F., & Boyaval, S. (2016). Unified formal reduction for fluid models of free surface shallow gravity-flows. *European Journal of Mechanics B/Fluids*, 55(1), 116–131. doi:10.1016/j.euromechflu.2015.09.003

Burger, J., Haldenwang, R., & Alderman, N. (2010). Friction factor-Reynolds number relationship for laminar flow of non-Newtonian fluids in open channels of different cross-sectional shapes. *Chemical Engineering Science.* 85, 3549–3556. doi:10.1016/j.ces.2010.02.040

Carreau, P.J., DeKee, D., & Daroux, M. (1979). An analysis of the viscous behavior of polymeric solutions. *The Canadian Journal of Chemical Engineering*, 57, 135-140. doi:10.1002/cjce.5450570202

Chanson, H., Jarny, S., & Coussot, P. (2006). Dam Break Wave of Thixotropic Fluid. *Journal of Hydraulic Engineering.*, 132 (3), 280–293. doi:10.1061/(asce)0733-9429(2006)132:3(280)

Chen, C.L., & Ling, C.H. (1996). Granular-flow rheology: role of shear-rate number in transition regime. *Journal of Engineering Mechanics*, 122 (5), 469–480. doi:10.1061/(ASCE)0733-9399(1996)122:5(469)

Chen, C.L., & Ling, C.H. (1998). Rheological equations in asymptotic regimes of granular flow. *Journal of Engineering Mechanics*, 124 (3), 301–310. doi:10.1061/(ASCE)0733-9399(1998)124:3(301)

Coussot, P. (1994). Steady, laminar, flow of concentrated mud suspensions in open channel. *Journal of Hydraulic Research*, 32(4), 535–559. doi:10.1080/00221686.1994.9728354

Dandapat, B.S., & Mukhopadhyay, A. (2001). Waves on a film of power–law fluid flowing down an inclined plane at moderate Reynolds number. *Fluid Dynamics Research*, 29, 199–220. doi:10.1016/s0169-5983(01)00024-7

Dandapat, B.S., & Mukhopadhyay, A. (2003). Waves on the surface of a falling power-law fluid film. *International Journal of Non-Linear Mechanics*, 38(1), 21–38. doi: 10.1016/S0020-7462(01)00038-5

Di Cristo, C., Iervolino, M., & Vacca, A. (2013a). Boundary Conditions Effect on Linearized Mud-Flow Shallow Model. *Acta Geophysica*, 61(3), 649–667. doi: 10.2478/s11600-013-0108-2

Di Cristo, C., Iervolino, M., & Vacca, A. (2013b). On the applicability of minimum channel length criterion for roll waves in mud flows, *Journal of Hydrology and Hydromechanics*, 61(4), 286–292. doi: 10.2478/johh-2013-0036

Di Cristo, C., Iervolino, M., & Vacca, A. (2013c). Waves dynamics in a linearized mud-flow shallow model. *Applied Mathematical Sciences*, 7(8), 377–393. Retrieved from http://m-hikari.com/ams/ams-2013/ams-5-8-2013/vaccaAMS5-8-2013.pdf

Di Cristo, C., Iervolino, M., & Vacca, A. (2013d). Gravity-Driven Flow of a Shear-Thinning Power–Law Fluid over a Permeable Plane. *Applied Mathematical Sciences*, 7(33-36), 1623–1641. Retrieved from http://www.m-hikari.com/ams/ams-2013/ams-33-36-2013/vaccaAMS33-36-2013.pdf

Di Cristo, C., Iervolino, M., & Vacca, A. (2014). Applicability of Kinematic, Diffusion, and Quasi-Steady, *Journal of Hydrologic Engineering*, 19(5), 956–965. doi:10.1061/(ASCE) HE.1943-5584.0000881

Di Cristo, C., Iervolino, M., & Vacca, A. (2015). On the stability of gradually varying mudflows in open channels. *Meccanica*, 50, 963–979. doi:10.1007/s11012-014-0075-y

Dracos, T.A., & Glenne, B. (1967). Stability criteria for open-channel flow. *Journal of the Hydraulic Division*, 93(HY6), 79-101.

Fernandez-Nieto, E.D., Noble, P., & Vila, J.P. (2010). Shallow water equations for non-Newtonian fluids. *Journal Non-Newtonian Fluid Mechanics*, 165, 712–732. doi:10.1016/j. jnnfm.2010.03.008Forterre, Y., & O. Pouliquen (2003). Long-surface wave instability in dense granular flows, *Journal of Fluid Mechanics*, 486, 21–50. doi:10.1017/S0022112003004555

Gottlieb, S., & Shu, C.W. (1998). Total variation diminishing Runge–Kutta schemes. *Mathematics of Computation*, 67(221), 73–85. doi: 10.1090/S0025-5718-98-00913-2

Harten, A. (1983). High resolution schemes for hyperbolic conservation laws. *Journal of Computational Physics*, 49(3), 357–393. doi:10.1016/0021-9991(83)90136-5

Heining, C., & Aksel, N. (2010). Effects of inertia and surface tension on a power-law fluid flowing down a wavy incline. *International Journal of Multiphase Flow*, 36(11–12), 847–857. doi:10.1016/j.ijmultiphaseflow.2010.07.002

Hewitt, D.R., & Balmforth, N.J. (2013). Thixotropic gravity currents. *Journal of Fluid Mechanics*, 727, 56–82. doi:10.1017/jfm.2013.235

Huang, X., & Garcia, M.H. (1998). A Herschel-Bulkley model for mud flow down a slope. *Journal of Fluid Mechanics*, 374, 305–333. doi:10.1017/s0022112098002845

Hunt, M.L., Zenit, R., Campbell, C.S., & Brennen, C.E. (2002). Revisiting the 1954 suspension experiments of R.A. Bagnold. *Journal of Fluid Mechanics*, 452, 1–24. doi:10.1017/S0022112001006577

Hwang, C.C., Chen, J.L., Wang, J.S., & Lin, J.S. (1994). Linear stability of power law liquid film flows down an inclined plane. *Journal of Physics D: Applied Physics.*, 27, 2297–2301. doi:10.1088/0022-3727/27/11/008

Kang, F., & Chen, K.P. (1995). Nonlinear elastic instability of gravity-driven flow of a thin viscoelastic film down an inclined plane. *Journal of Non-Newtonian Fluid Mechanics*, 57(2-3), 243–252. doi:10.1016/0377-0257(94)01333-D

Kranenburg, C. (1990). On the stability of gradually varying flow in wide open channels. *Journal of Hydraulic Research*, 28(5), 621–628. doi:10.1080/00221689009499050

Lin, J.S., & Hwang, C.C. (2000). Finite amplitude long-wave instability of power-law liquid films. *International Journal of Non-Linear Mechanics*, 35(5), 769–777. doi:10.1016/S0020-7462(99)00056-6

Liu, K.F., & Mei, C.C. (1989). Slow spreading of Bingham fluid on an inclined plane. *Journal of Fluid Mechanics*, 207, 505–529. doi:10.1017/S0022112089002685

Liu, K.F. & Mei, C.C. (1990). Approximate equations for the slow spreading of a thin sheet Bingham plastic fluid. *Physics of Fluids A,* 2, 30–36. doi:10.1063/1.857821

Longo, S. (2011). Roll waves on a shallow layer of a dilatant fluid. *European Journal of Mechanics B/Fluids*, 30(1), 57–67. doi:10.1016/j.euromechflu.2010.09.001

Longo, S., Di Federico, V. & Chiapponi, L. (2015). Non-Newtonian power-law gravity currents propagating in confining boundaries. *Environmental Fluid Mechanics*, 15(3), 515–535. doi:10.1007/s10652-014-9369-9

Mei, C.C., & Yuhi, M. (2001). Slow flow of a Bingham fluid in a shallow channel of finite width. *Journal of Fluid Mechanics*, 431, 135–159. doi:10.1017/S0022112000003013

Miladinova, S., Lebon, G., & Toshev, E. (2004). Thin-film flow of a power-law liquid falling down an inclined plate. *Journal of Non-Newtonian Fluid Mechanics*, 122, 69–78. doi:10.1016/j.jnnfm.2004.01.021

Ng, C., & Mei, C.C. (1994). Roll waves on a shallow layer of mud modeled as a power-law fluid. *Journal of Fluid Mechanics*, 263, 151–184. doi:10.1017/s0022112094004064

Noble, P., & Villa, J. (2013). Thin power-law film flow down an inclined plane: consistent shallow-water models and stability under large-scale perturbations. *Journal of Fluid Mechanics*, 735, 29-60. doi:10.1017/jfm.2013.454

Pascal, J.P. (2006). Instability of power-law fluid flow down a porous incline. *Journal Non-Newtonian Fluid Mechanics*, 133, 109–120. doi:10.1016/j.jnnfm.2005.11.007

Pascal, J.P., & D'Alessio, S.J.D. (2007). Instability of power-law fluid flows down an incline subjected to wind stress. *Applied Mathematical Modelling*, 31(7), 1229–1248. doi:10.1016/j.apm.2006.04.002

Paz, R.R., Storti, M.A., & Garelli, L. (2011). Local absorbent boundary condition for non-linear hyperbolic problems with unknown Riemann invariants, *Computers & Fluids*, 40(1), 52–67. doi:10.1016/j.compfluid.2010.08.001

Pinkerton, H., & Sparks, R.S.J. (1978). Field measurements of the rheology of lava. *Nature*, 276, 383–385. doi:10.1038/276383a0

Ruyer-Quil, C., & Manneville, P. (1998). Modeling film flows down inclined plane. *European Physical Journal* B, 6(2), 277–298. doi:10.1007/s100510050550

Ruyer-Quil, C., & Manneville, P. (2000). Improved modeling of flows down inclined plane. *European Physical Journal* B B, 15(2), 357–369. doi:10.1007/s100510051137

Sadiq, I.M.R., & Usha, R. (2010). Effect of permeability on the instability of a non-Newtonian film down a porous inclined plane. *Journal of Non-Newtonian Fluid Mechanics*, 165, 1171–1188. doi:10.1016/j.jnnfm.2010.06.002

Smith, M.K. (1990). The mechanism for the long-wave instability in thin liquid film. *Journal of Fluid Mechanics*, 217, 469–485. doi:10.1017/s0022112090000805

Sonder, I., Zimanowski, B., & Buttner, R. (2006). Non-Newtonian viscosity of basaltic magma. *Geophysical Research, Letters,* 33, L02303. doi:10.1029/2005GL024240

Takahashi, T. (1991). *Debris Flow*. IAHR Monograph Series. Balkema, Rotterdam, The Netherlands.

Tamburrino, A., & Ihle, C.F. (2013). Roll wave appearance in bentonite suspensions flowing down inclined planes. *Journal of Hydraulic Research*, 51(3), 330–335. doi:10.1080/00221686.2013.769468

Trowbridge, J.H. (1987). Instability of concentrated free surface flow. *Journal of Geophisical Research*, 92, c9, 9523–9530. doi:10.1029/JC092iC09p09523

Uma, B. (2012). Effect of Wind Stress on the Dynamics and Stability of Nonisothermal Power-Law Film down an Inclined Plane. *ISRN Mathematical Physics*, 2012, Article ID 732675. doi:10.5402/2012/732675

Usha, R., Millet, S., Ben Hadid, H., & Rousset, F. (2011). Shear-thinning film on a porous substrate: Stability analysis of a one-sided model. *Chemical Engineering Science*, 66(22), 5614–5627. doi:10.1016/j.ces.2011.07.041

Wang, Z.-Y. (2002). Free surface instability of non-Newtonian laminar flows. *Journal of Hydraulic Research*, 40, 449–460. doi: 10.1080/00221680209499887

Witham, G.B. (1974). *Linear and nonlinear waves*. John Wiley & Sons Interscience, New York.

Zhang, X., Bai, Y., & Ng, C.O. (2010). Rheological properties of some marine muds dredged from China coasts. In: *Proceedings of the 28th International Offshore and Polar Engineering Conference*, Beijing, China, 455–461.

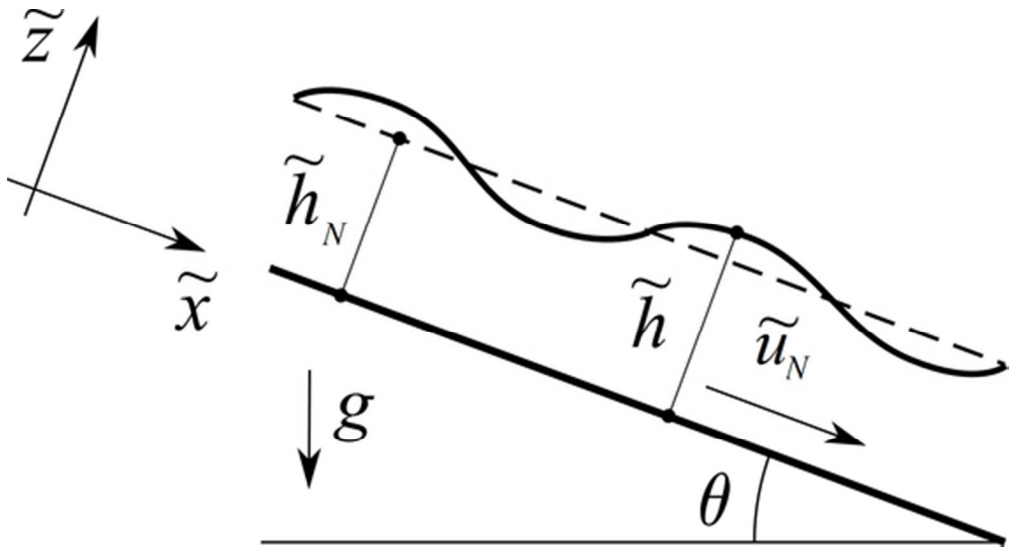

48x25mm (300 x 300 DPI)

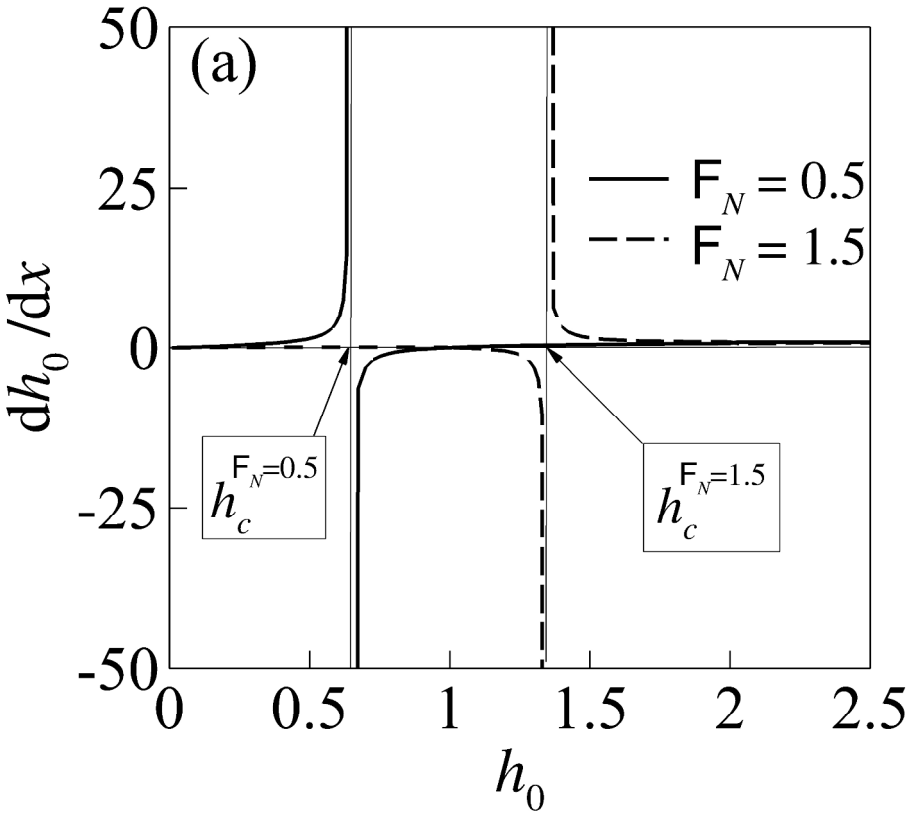

Fig. 2a
793x705mm (96 x 96 DPI)

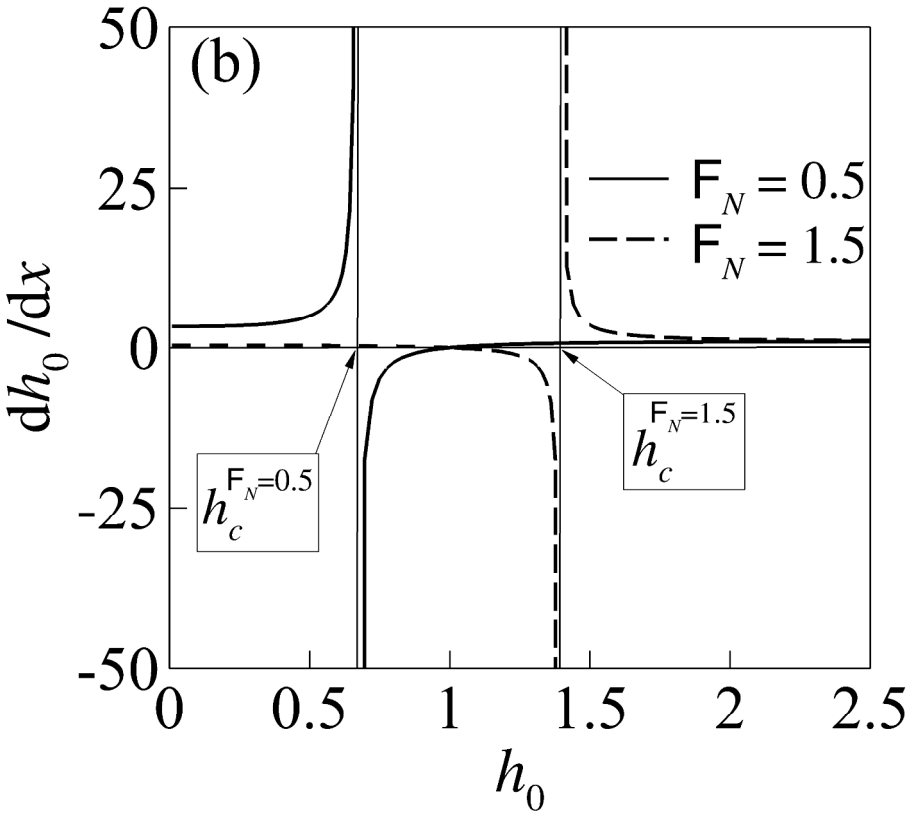

Fig. 2b
793x705mm (96 x 96 DPI)

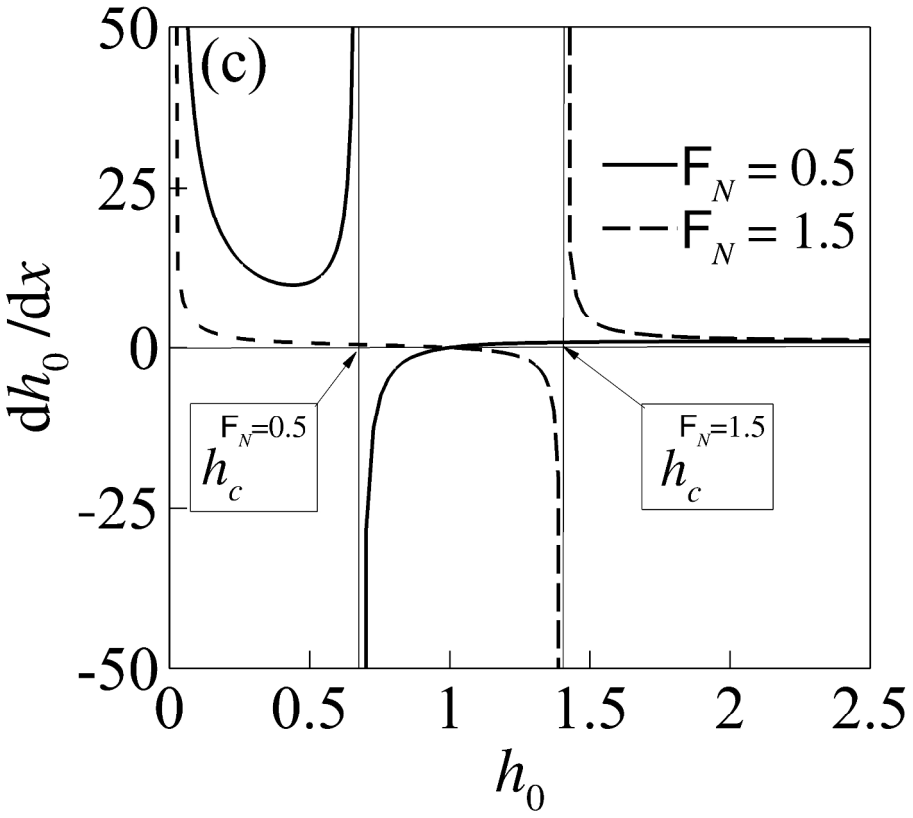

Fig. 2c
793x705mm (96 x 96 DPI)

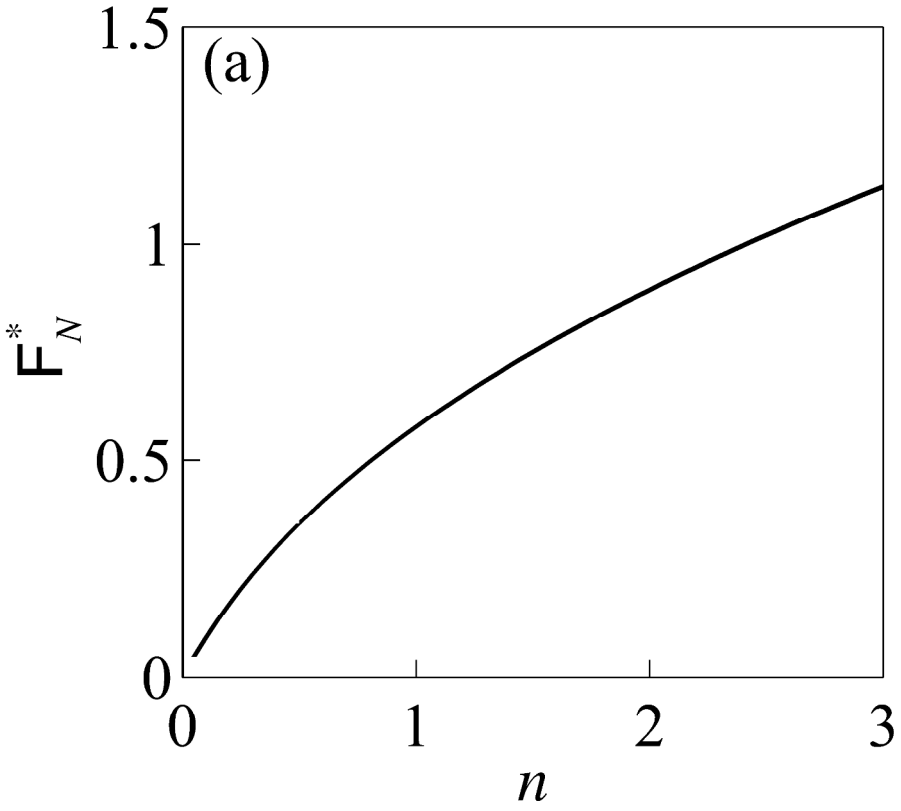

Fig. 3a
793x705mm (96 x 96 DPI)

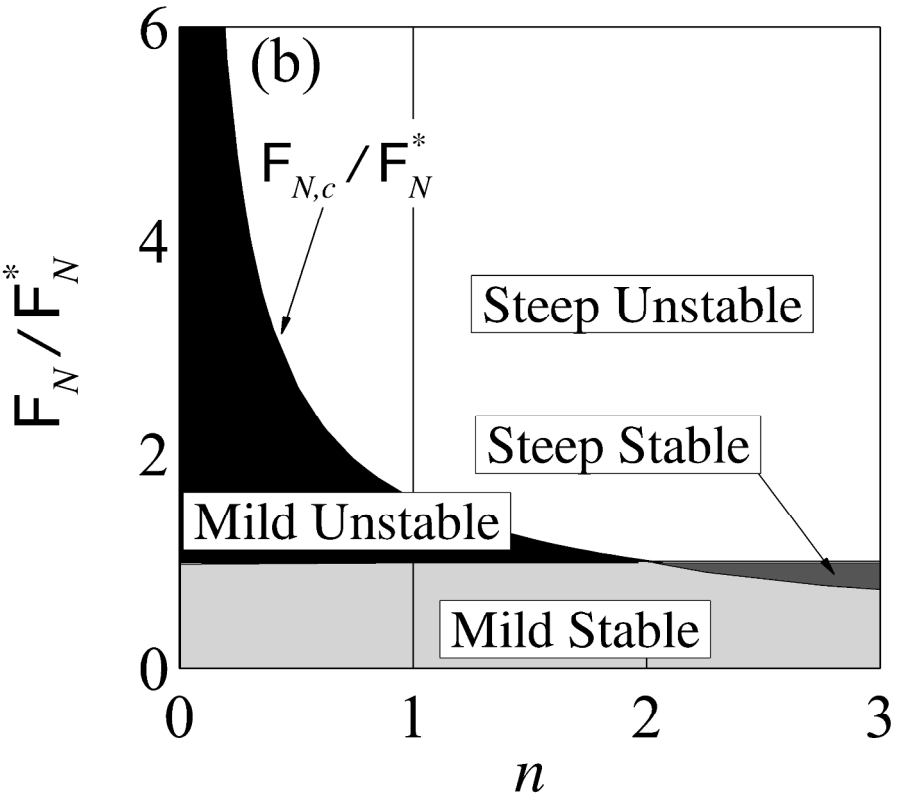

Fig. 3b
793x705mm (96 x 96 DPI)

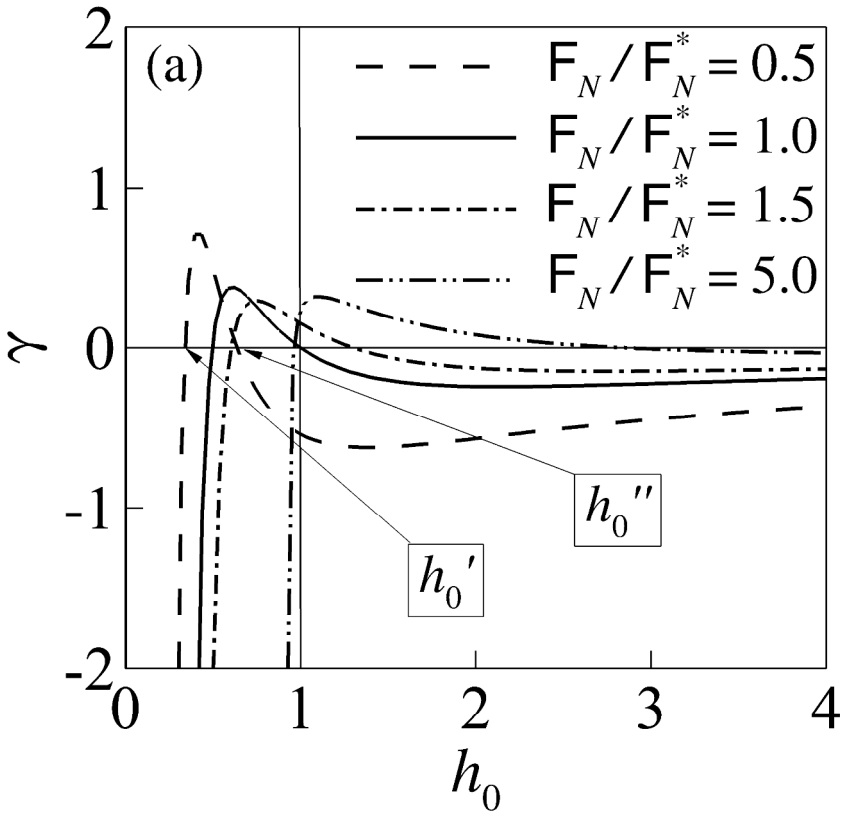

Fig. 4a
793x705mm (96 x 96 DPI)

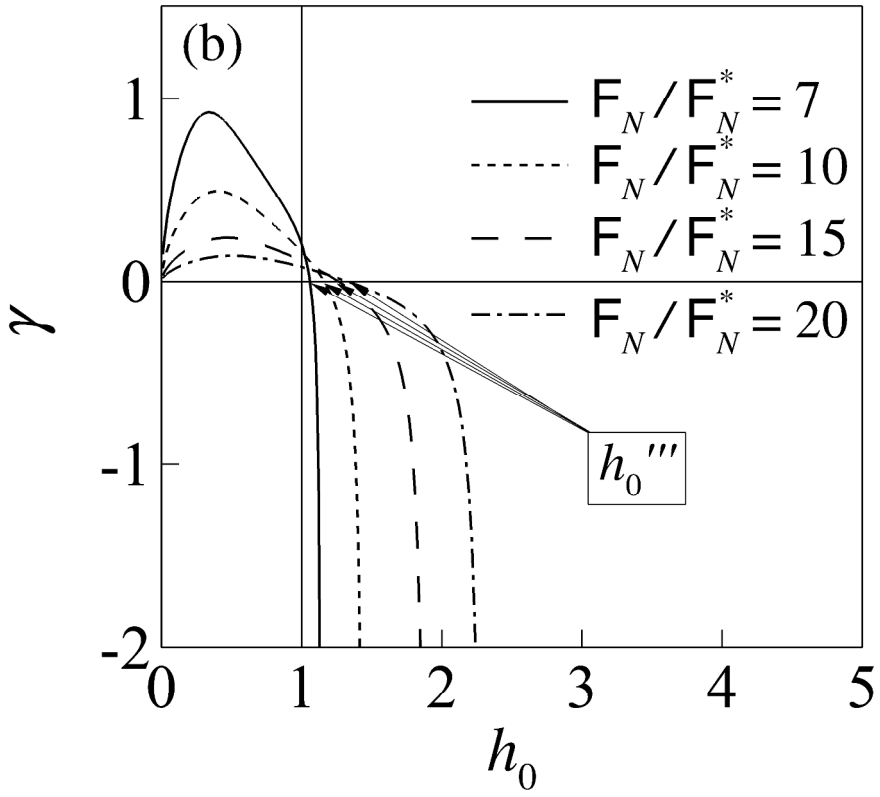

Fig. 4b
793x705mm (96 x 96 DPI)

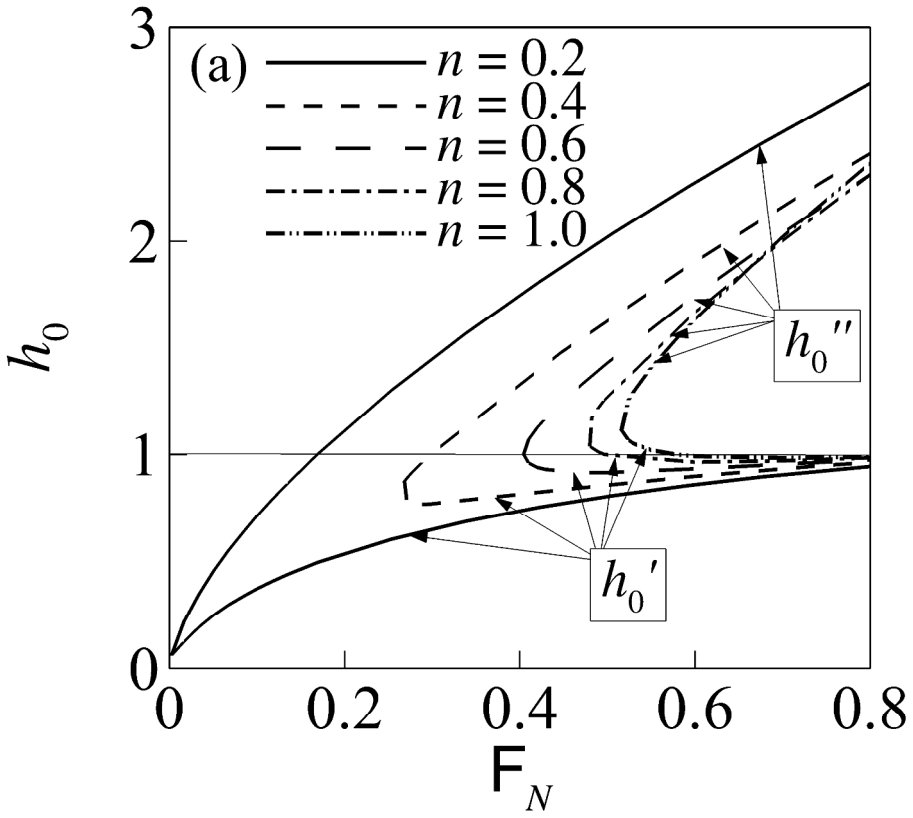

Fig. 5a
793x705mm (96 x 96 DPI)

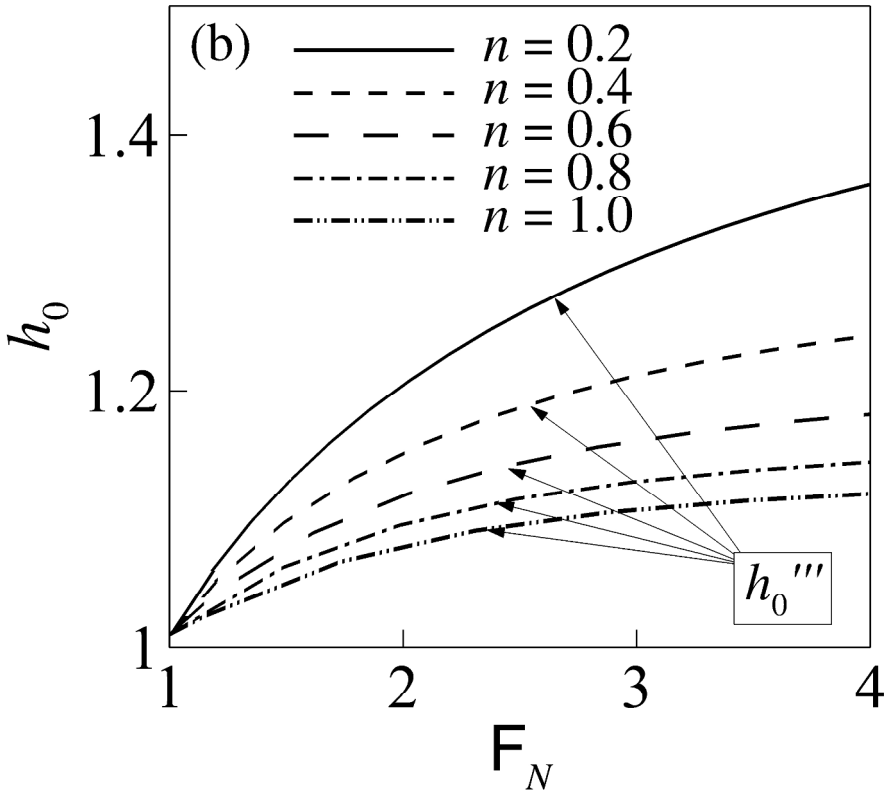

Fig. 5b
793x705mm (96 x 96 DPI)

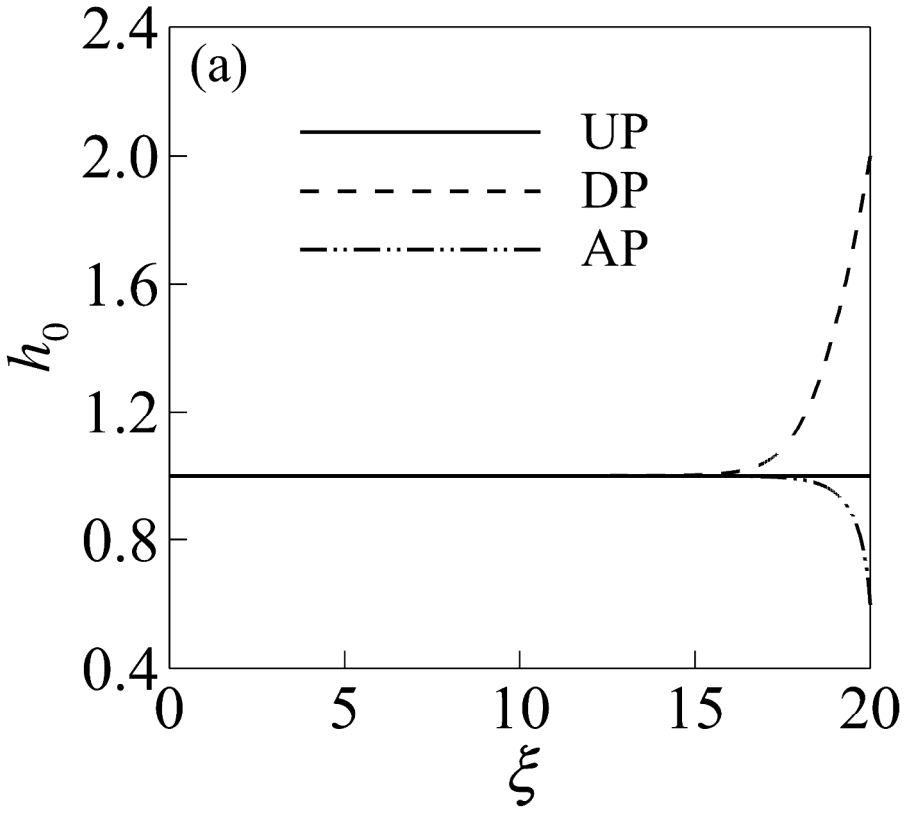

Fig. 6a
793x705mm (96 x 96 DPI)

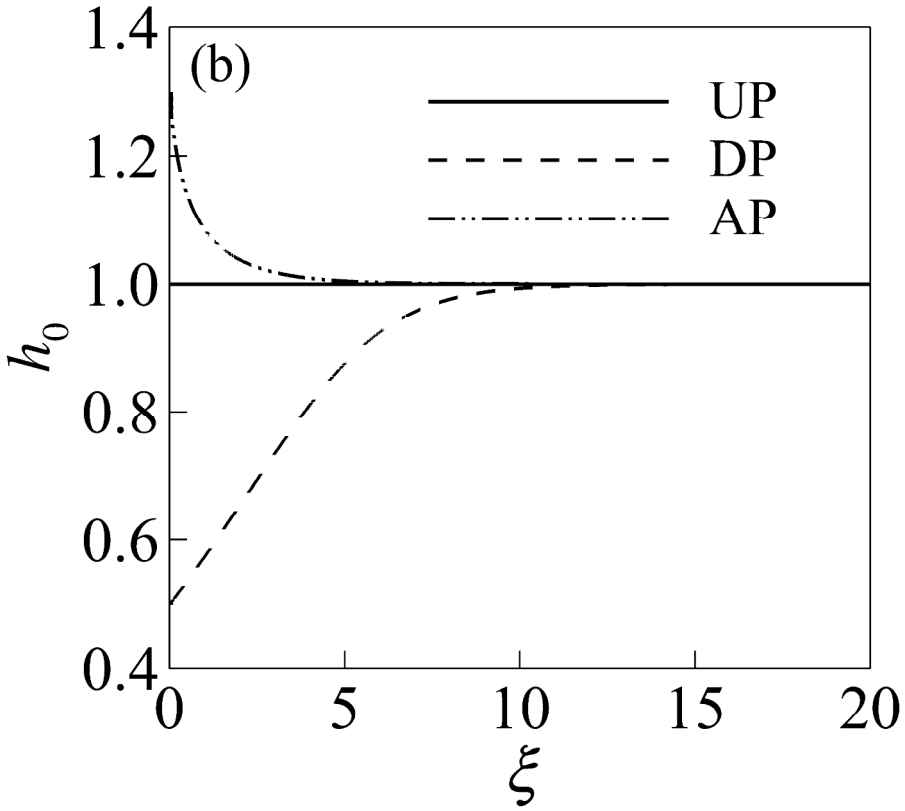

Fig. 6b
793x705mm (96 x 96 DPI)

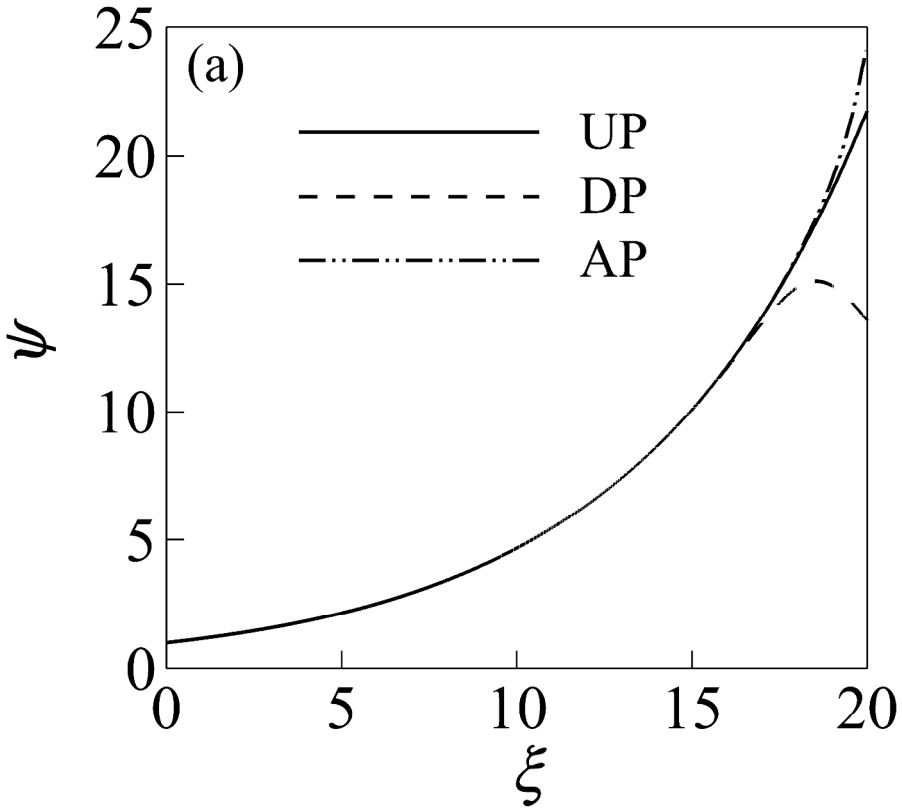

Fig. 7a
793x705mm (96 x 96 DPI)

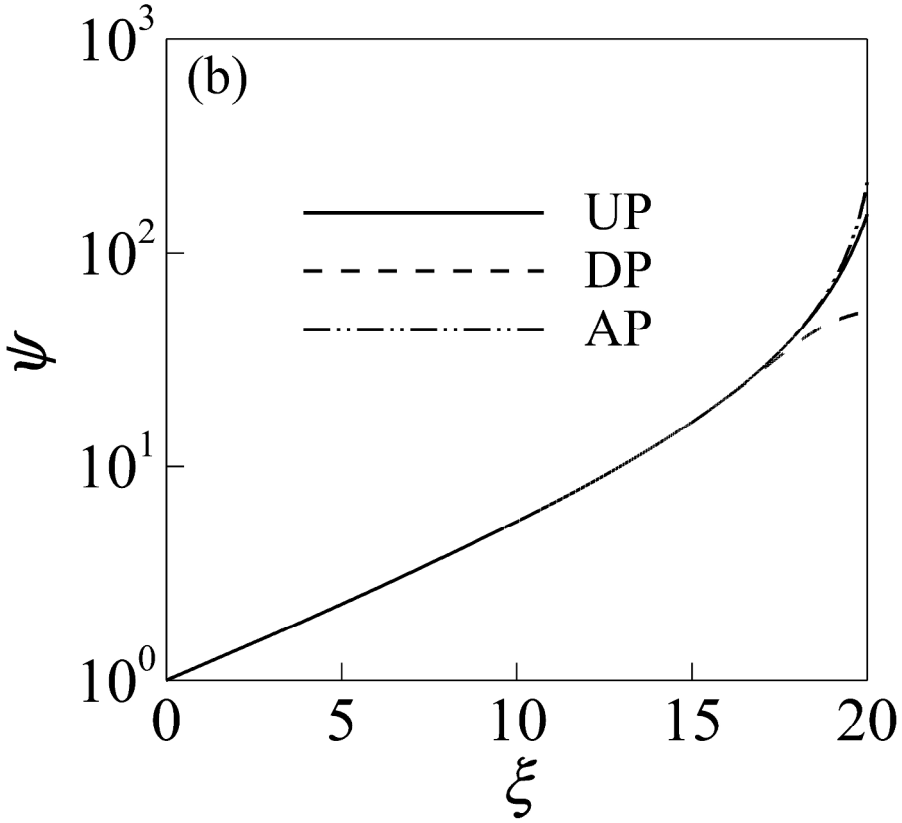

Fig. 7b
793x705mm (96 x 96 DPI)

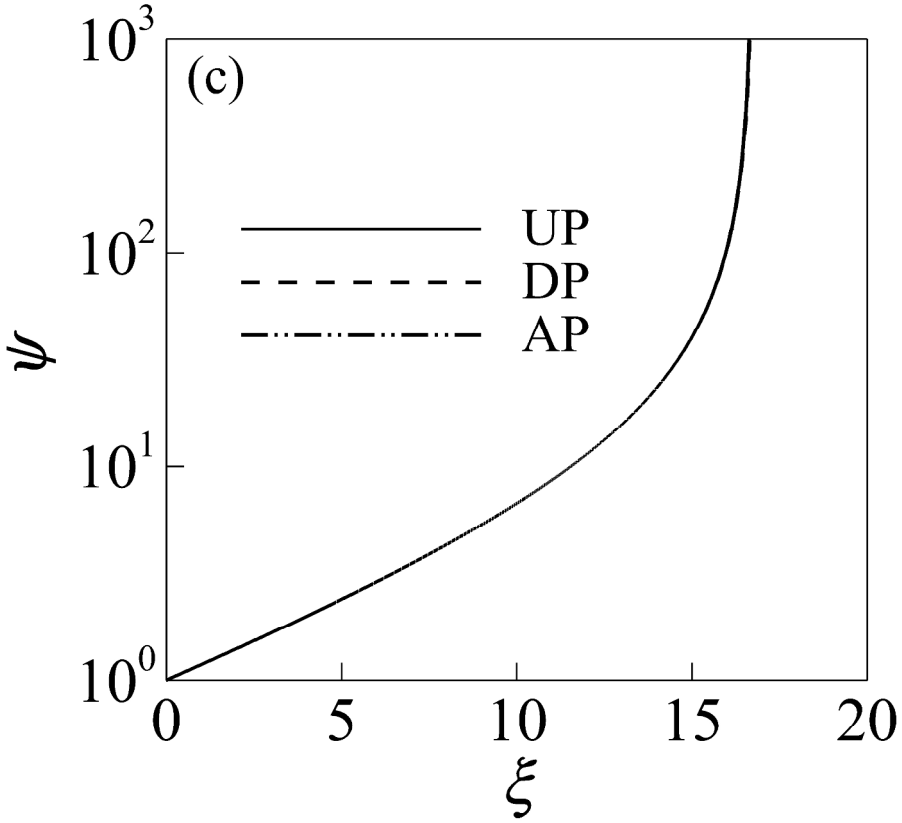

Fig. 7c
793x705mm (96 x 96 DPI)

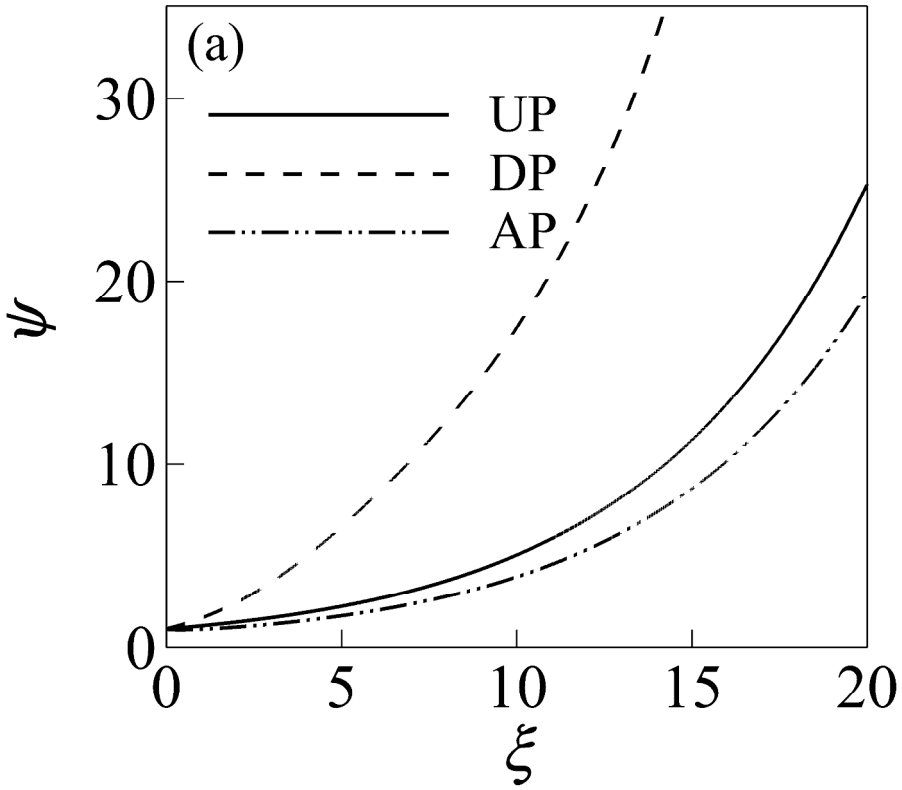

Fig. 8a
793x705mm (96 x 96 DPI)

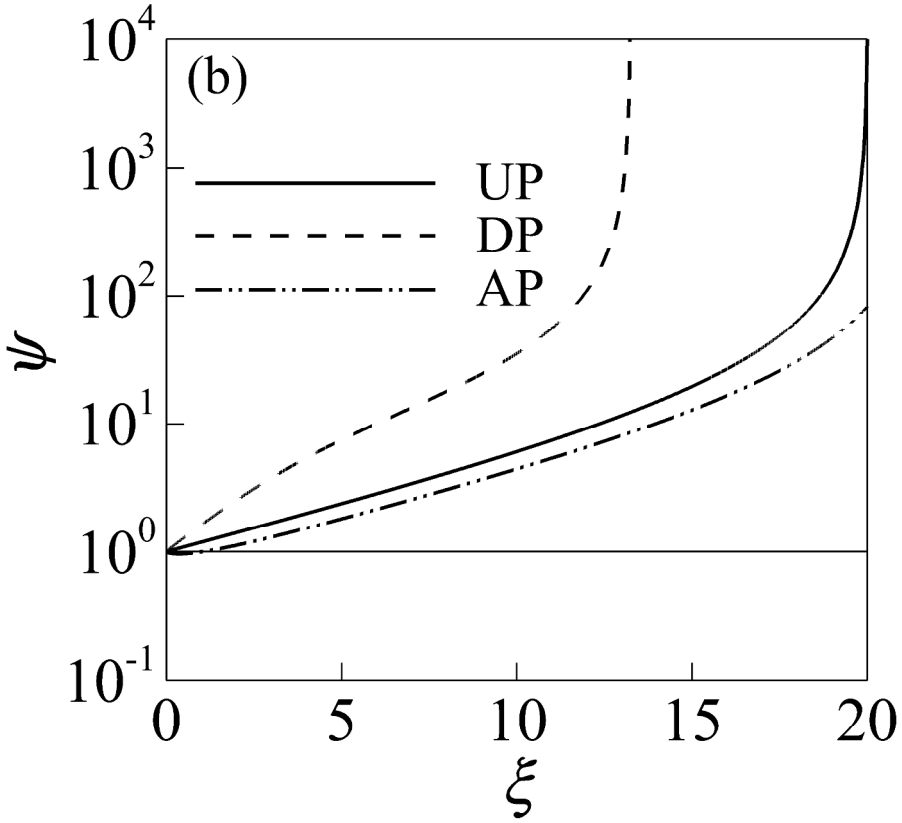

Fig. 8b
793x705mm (96 x 96 DPI)

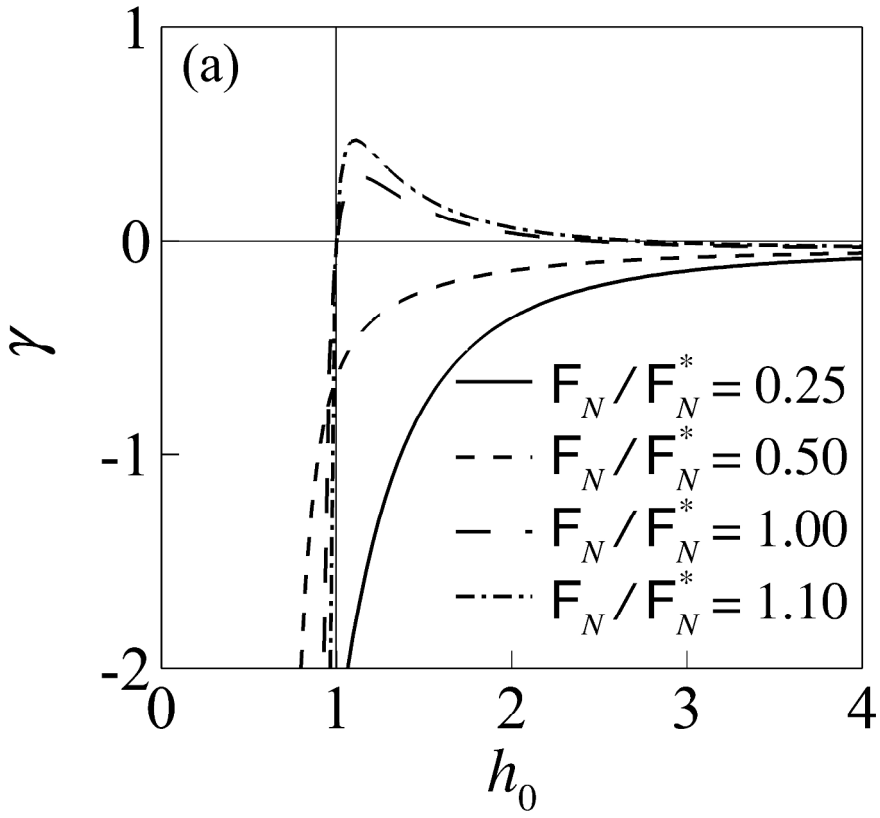

Fig. 9a
793x705mm (96 x 96 DPI)

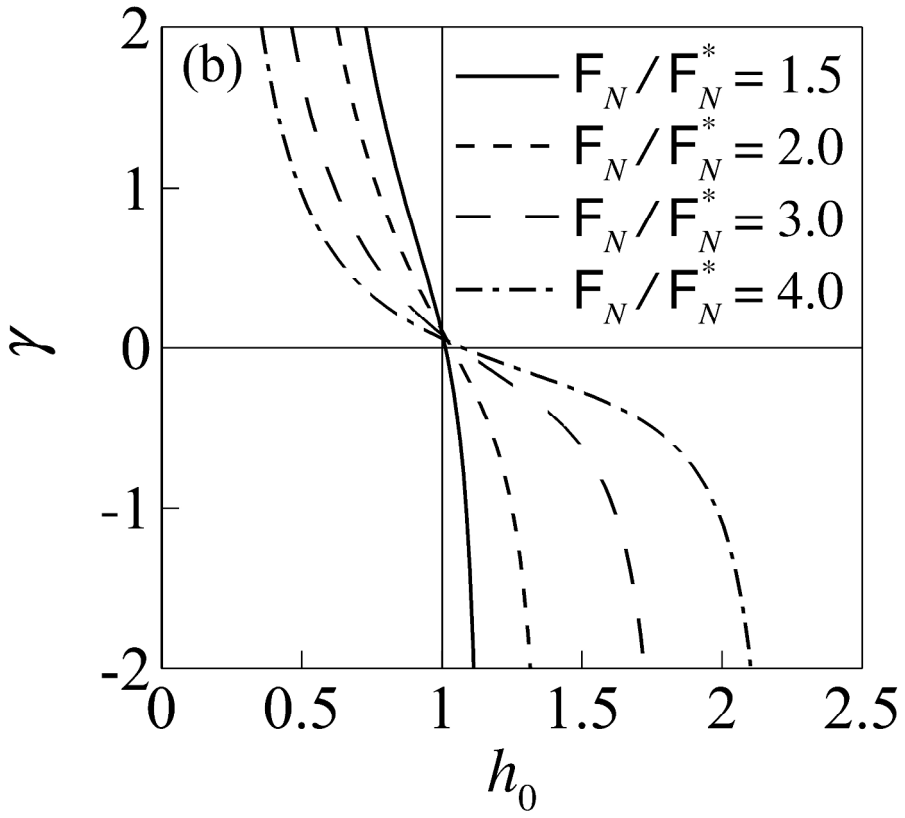

Fig. 9b
793x705mm (96 x 96 DPI)

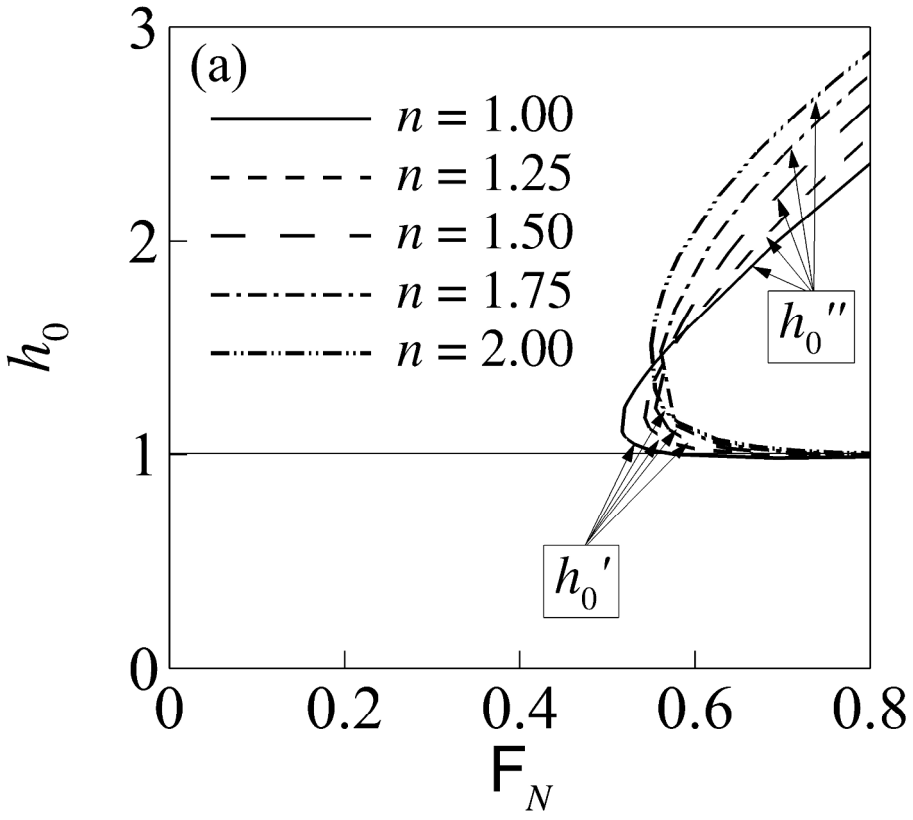

Fig. 10a
793x705mm (96 x 96 DPI)

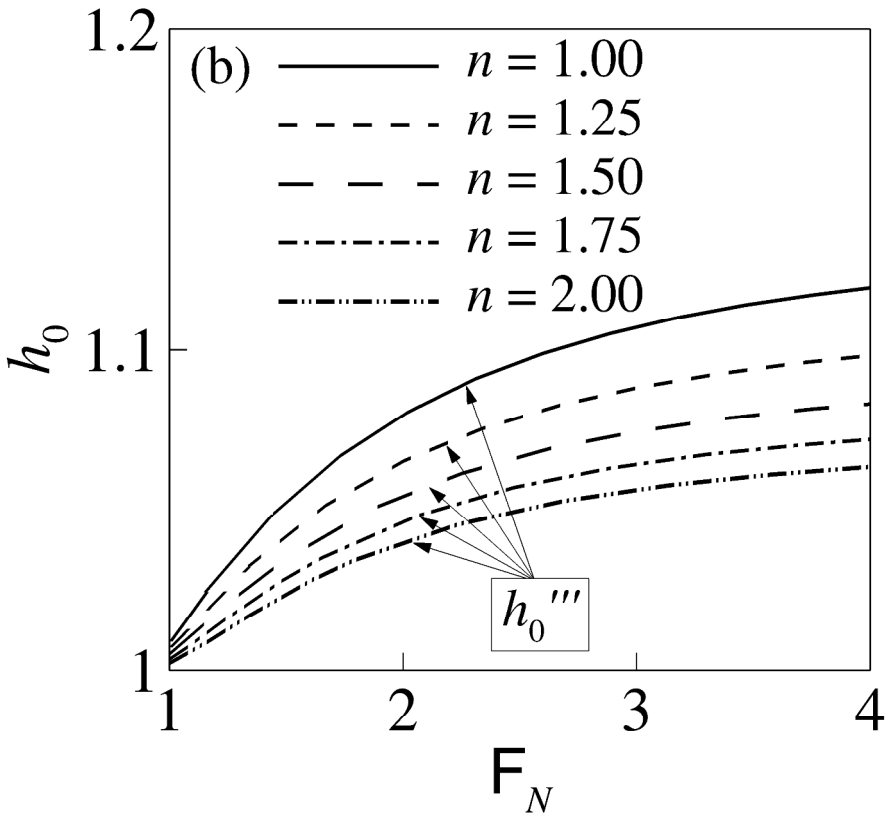

Fig. 10b
793x705mm (96 x 96 DPI)

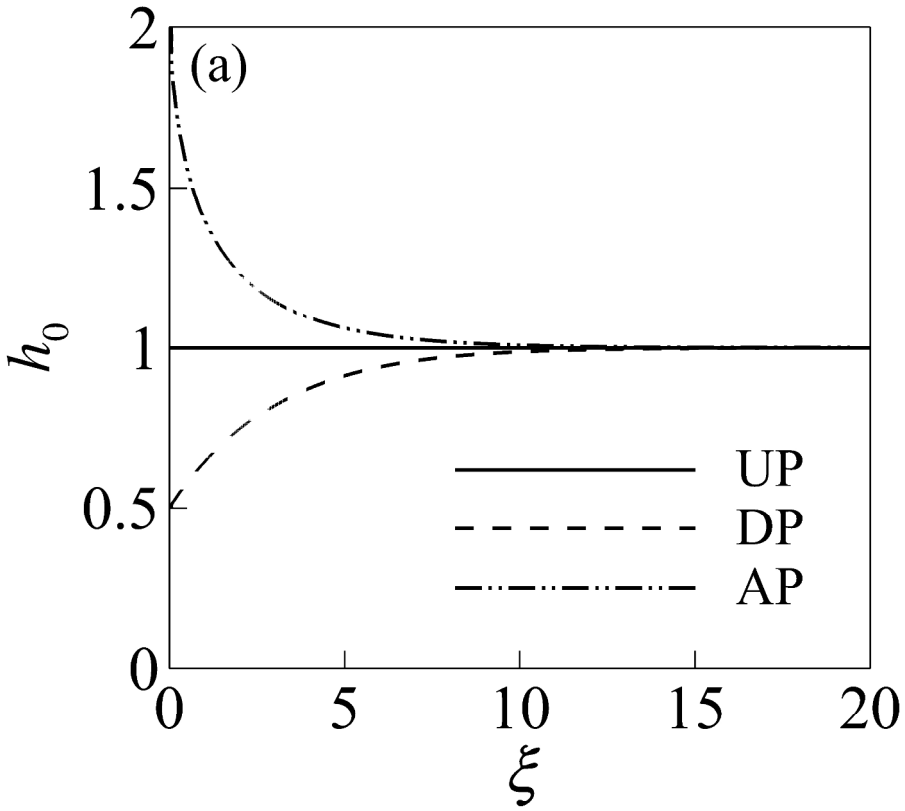

Fig. 11a
793x705mm (96 x 96 DPI)

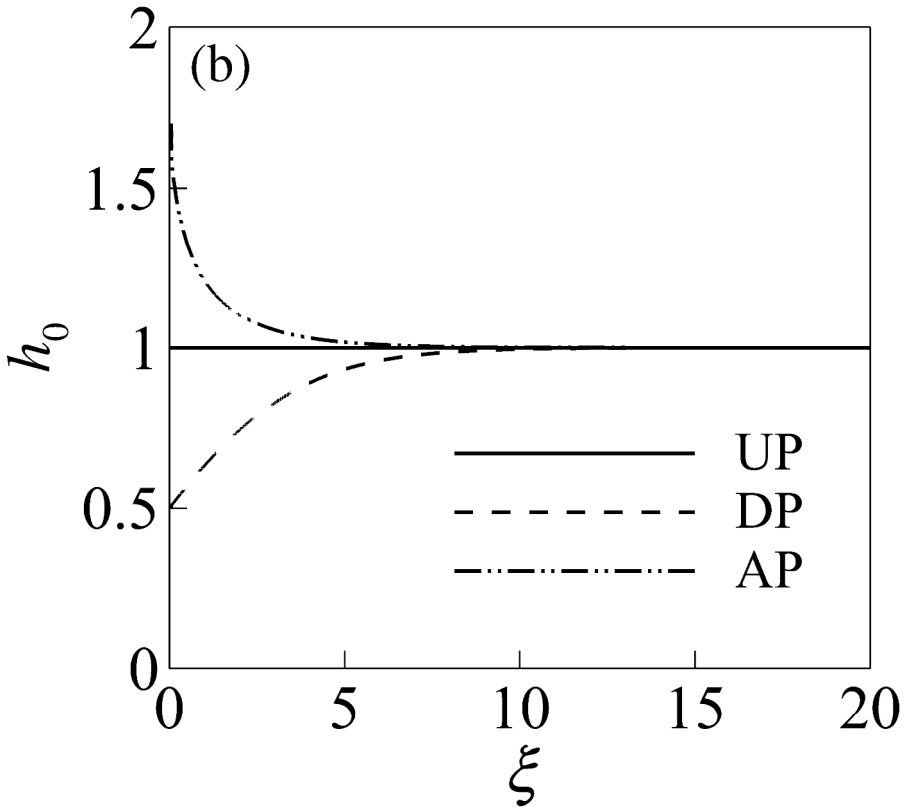

Fig. 11b
793x705mm (96 x 96 DPI)

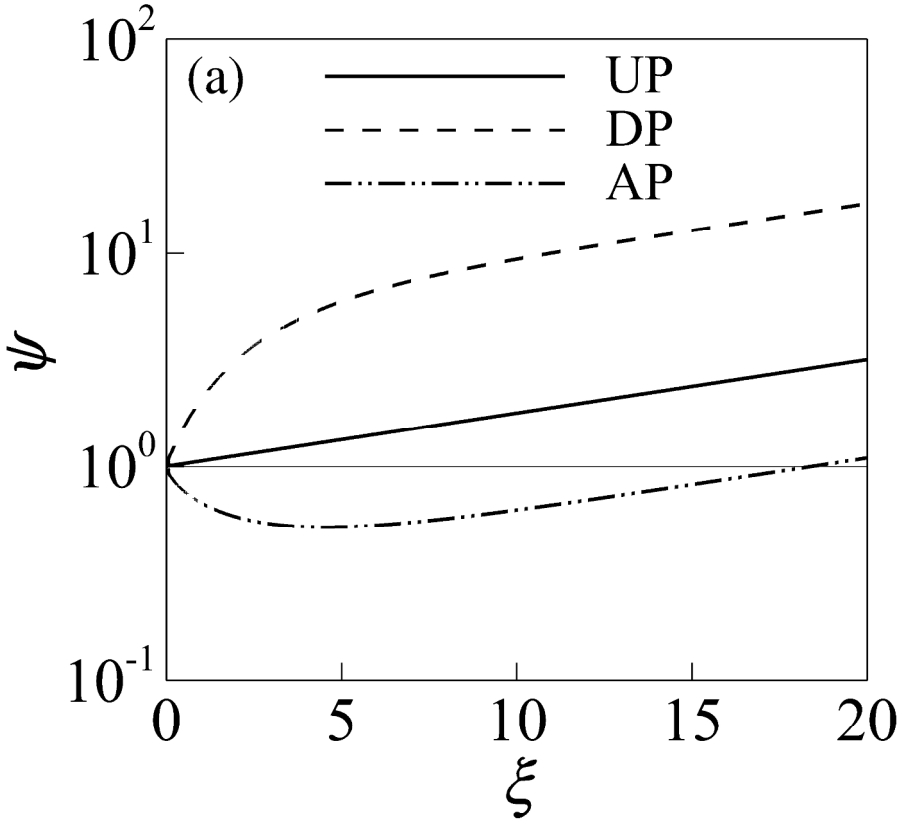

Fig. 12a
793x705mm (96 x 96 DPI)

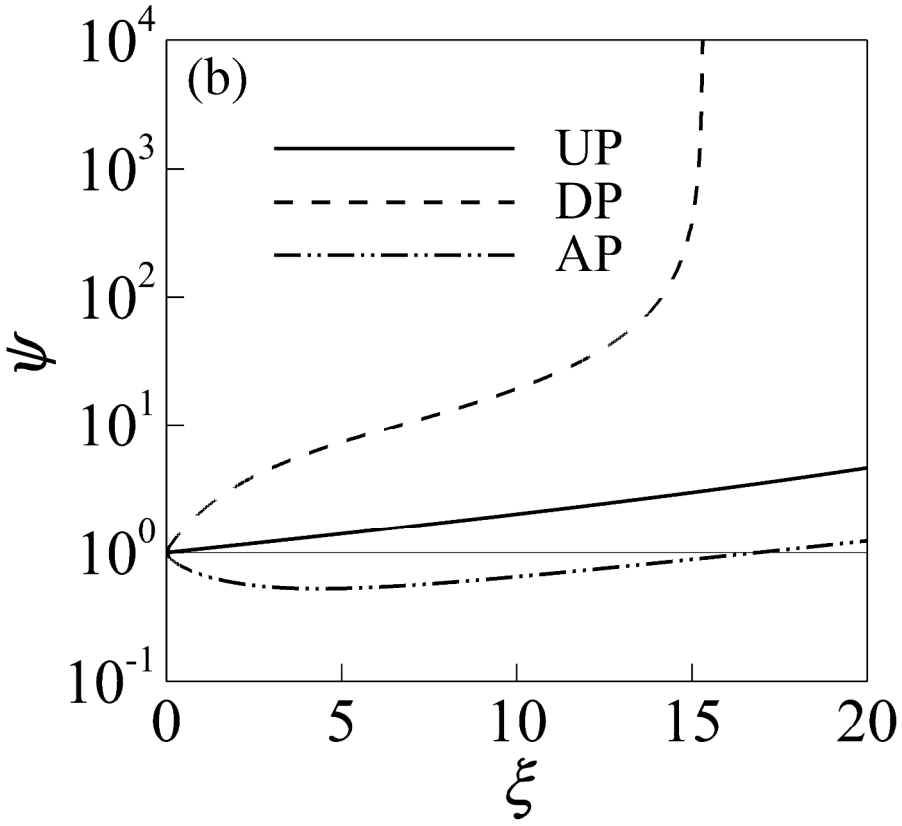

Fig. 12b
793x705mm (96 x 96 DPI)

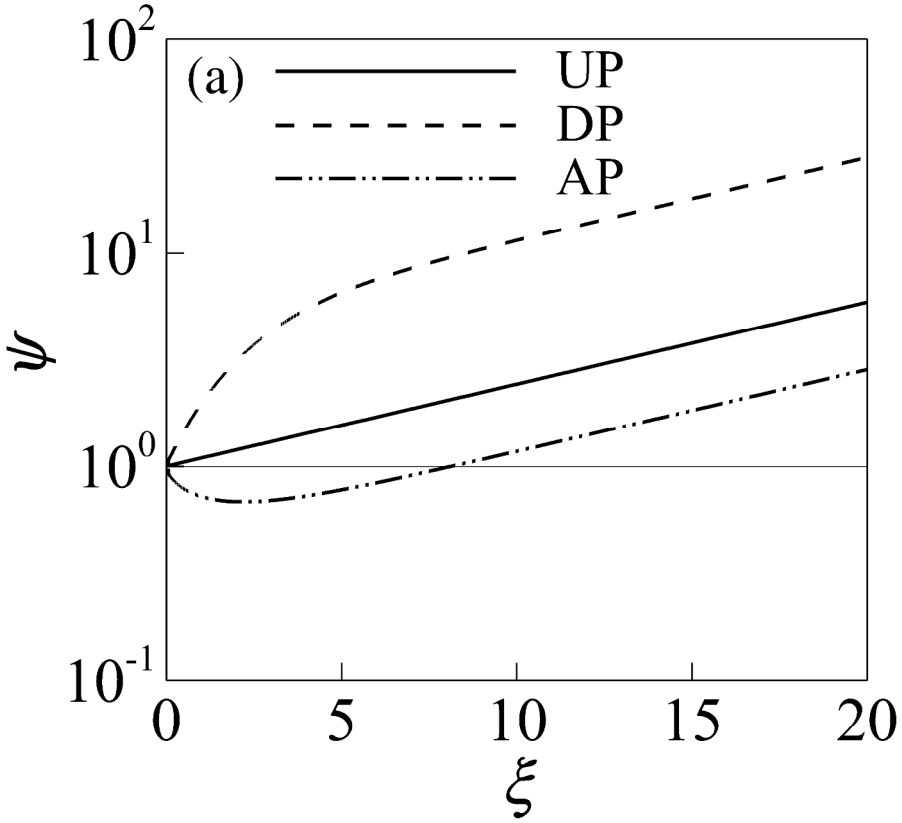

Fig. 13a
793x705mm (96 x 96 DPI)

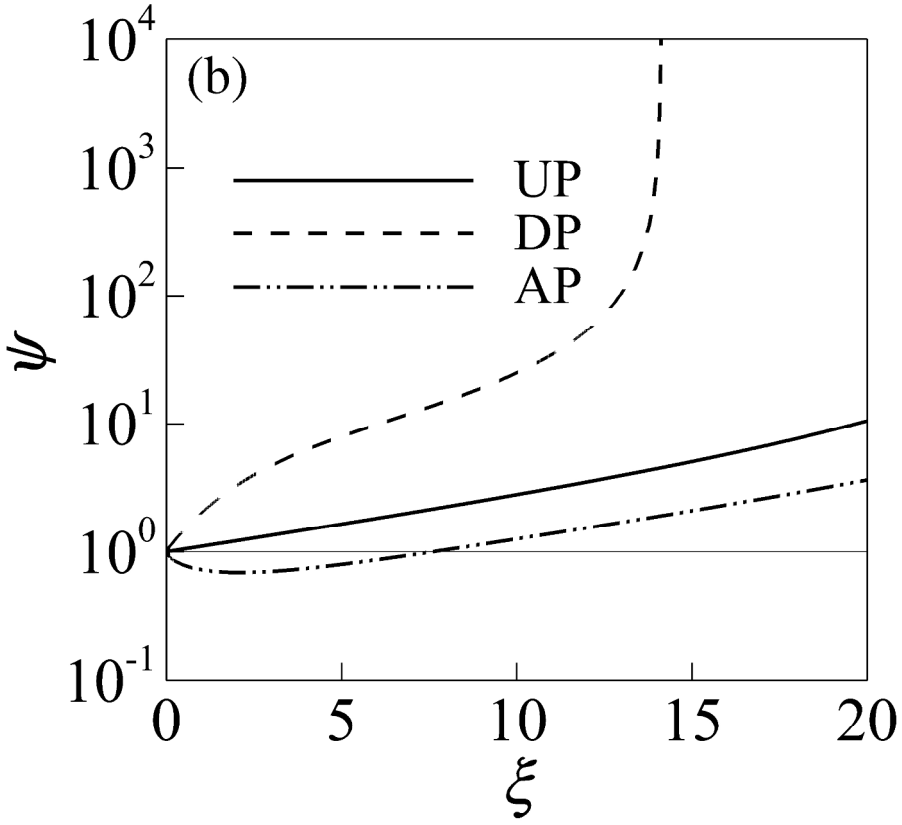

Fig. 13b
793x705mm (96 x 96 DPI)

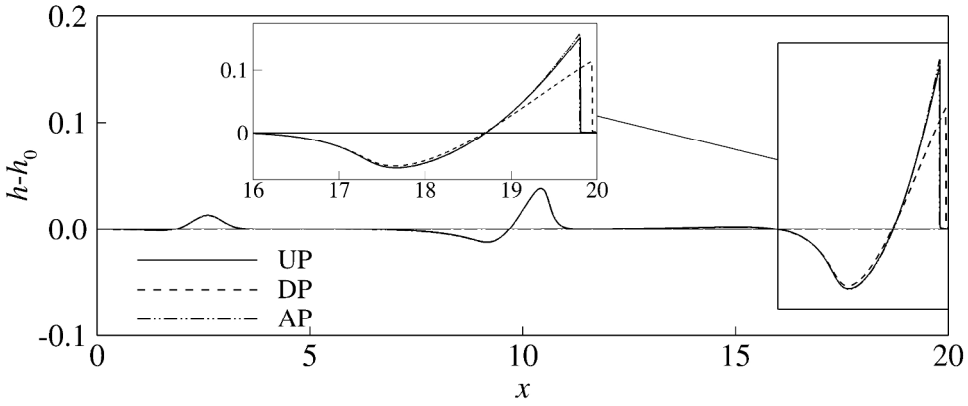

Fig. 14
793x352mm (96 x 96 DPI)

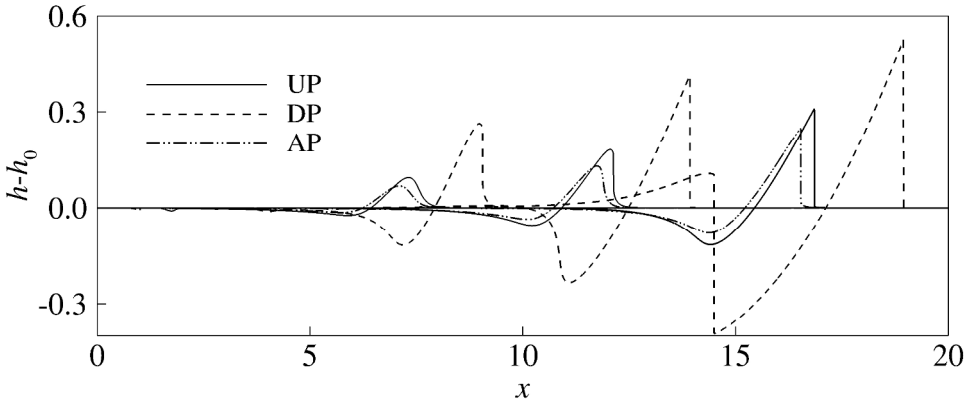

Fig. 15
793x352mm (96 x 96 DPI)

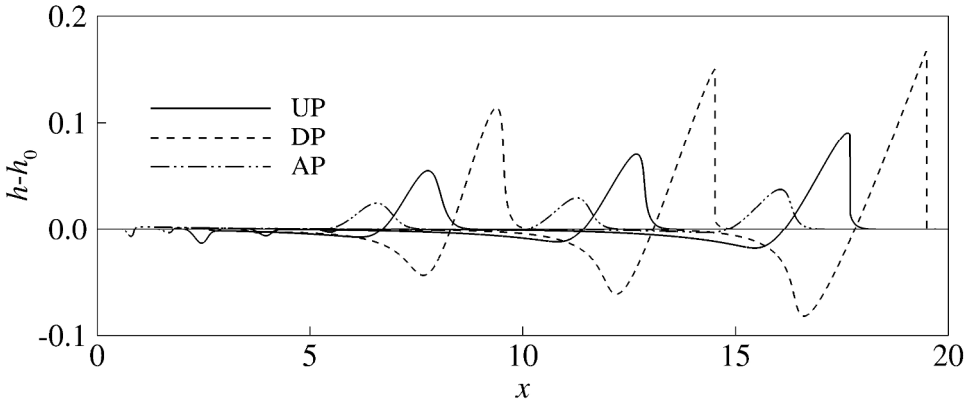

Fig. 16
793x352mm (96 x 96 DPI)

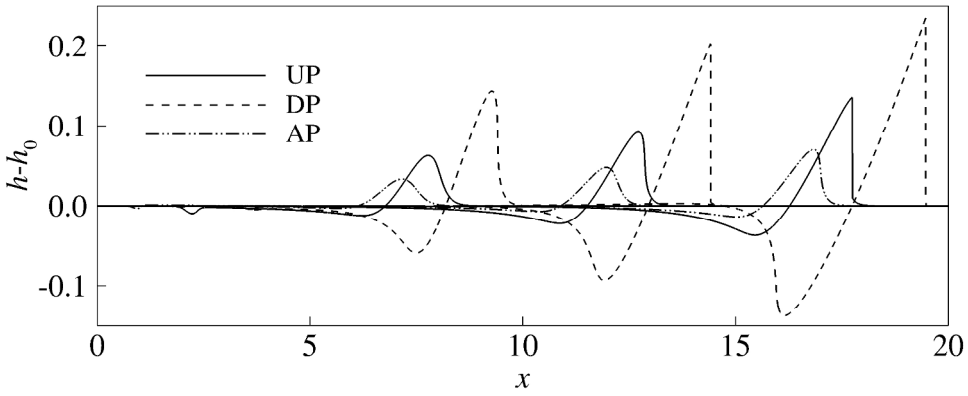

Fig. 17
793x352mm (96 x 96 DPI)

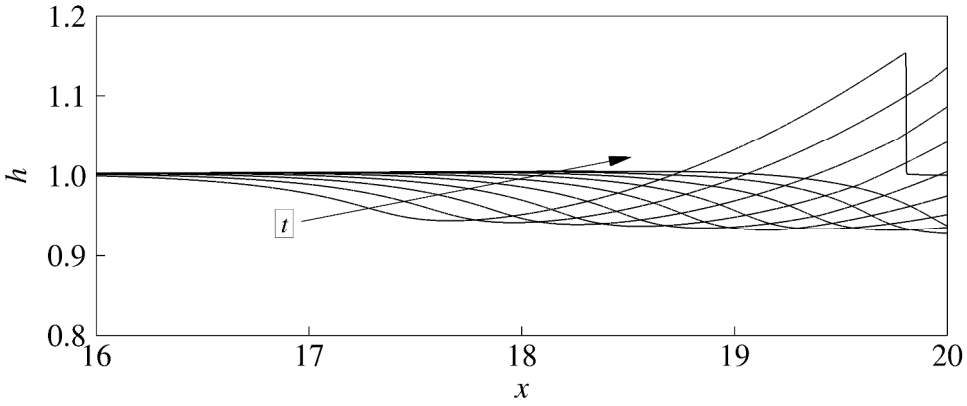

Fig. A1
793x352mm (96 x 96 DPI)